RESEARCH



Laser induced grating spectroscopy measurements of temperature and water vapour in turbulent lean premixed methane-hydrogen-air flames at pressure

Lee Weller¹ · Anthony Giles² · Oussama Chaib¹ · Steve Morris² · Benjamin A. O. Williams³ · Simone Hochgreb¹

Received: 4 June 2025 / Accepted: 15 September 2025 © The Author(s) 2025

Abstract

This study explores the application of Laser-Induced Grating Spectroscopy (LIGS) for non-intrusive measurements of temperature and water vapour concentration in premixed flames of air with blends of hydrogen and methane under high-pressure conditions. Employing a swirl-stabilized burner, the research demonstrates the capabilities of tracer-free LIGS, using thermal and electrostrictive gratings generated by a 1064 nm Nd:YAG laser, to measure local temperatures and water molar fractions. The study also includes an extension of the thermoacoustic model for characteristics LIGS signals, built in order to extract the relative concentration of water vapour from the ratio of second (thermal) to first (electrostrictive) peak magnitudes. Experiments are conducted in non-sooting flames, leveraging a high-pressure optical chamber (HPOC) with pressures up to 3 bar. The study evaluates mixtures of methane and hydrogen (100%, 70%, and 40% CH₄) and identifies key relationships between LIGS signal characteristics, frequency distributions, and combustion dynamics. Results show excellent agreement between measured temperatures and adiabatic flame temperatures, alongside measurements of water vapour molar fractions. The spatial temperature and water vapour maps are related to the complex mixing and recirculation patterns associated with the flame's shear and recirculation zones. The results establish LIGS as a robust diagnostic tool for combustion analysis, with potential applications in advancing hydrogen-rich energy systems.

1 Introduction

Accurate non-intrusive spatial-temporal measurements of key scalars such as temperature and species concentration in combustion environments are very important in understanding the structure and stability of pressurized turbulent flames. Specifically, hydrogen has attracted particular attention in the last decade as a flexible energy carrier and a carbon-free alternative to conventional fuels used in modern gas turbines and aero-engines. Hydrogen offers high calorific value per unit mass, wide flammability limits and

premixed laminar flame speeds about 2-5 times faster than hydrocarbons in the lean range, leading to shorter and more compact flames [1–4]

A number of studies have by now indicated that the substitution of hydrogen for methane in blends is feasible without a significant change to the combustion process for volumetric fractions of hydrogen of up to 70% [1–3]. Beyond that value, however, hydrogen properties dominate, and the mixture becomes prone to flashback and instabilities. In this study, we focus on mixtures below 70% hydrogen, which would likely be used in lowering the carbon footprints of power plants if green hydrogen is available. In general, it is important to map out not only the mean temperatures produced, but also the instantaneous probability distribution functions of temperature produced by burners across a range of hydrogen/methane mixtures, in order to generate realistic predictions of NO production.

Laser diagnostics in combustion environments aim to achieve precise and accurate non-intrusive in-situ measurements of temperature and species concentration with high spatial and temporal resolution. A number of different

Published online: 06 October 2025



[☐] Lee Weller lw493@cam.ac.uk

Department of Engineering, University of Cambridge, Cambridge CB2 1PZ, UK

School of Engineering, Cardiff University, Cardiff CF24 3AA, UK

Department of Engineering, University of Oxford, Oxford OX1 3PJ, UK

techniques have been developed to fulfil this purpose. These range from incoherent techniques such as Rayleigh or Raman scattering [5–8], to line techniques such as laser induced fluorescence [9], and coherent techniques such as Coherent Anti-Stokes Raman Scattering (CARS), Degenerate Four-Wave Mixing (DFWM) [10] and Laser-Induced Grating Spectroscopy (LIGS). Of the incoherent techniques, spontaneous Raman and LIF are appropriate for high temperature, high pressure environments for thermometry but substantial calibration work is required to obtain accurate results. Of the coherent techniques, LIGS is the simplest, and requires significantly less expertise and equipment than a comparably accurate CARS technique for purposes of thermometry. LIGS has been used primarily to measure temperatures, but in some cases also to extract pressure, velocity, and molar concentration in both reacting and nonreacting flows, as documented in various studies [10–14]. Spatially resolved measurements of water vapor concentrations are particularly difficult in combustion diagnostics, as the molecular Raman cross sections are relatively small. A number of fs-CARS studies have highlighted some of those difficulties [15–17]. The present paper builds on previous work on using the ratio of thermal to electrostrictive peaks in LIGS for extraction of vapor concentrations [18], along with temperature measurements.

A LIGS signal is generated in the form of an unsteady, coherent signal beam arising from an incident laser beam scattering off a stationary density perturbation interacting with a moving pressure wave. Its special feature is that the frequency of the scattered signal can be measured with high precision, and this reveals the speed of a sound wave. The thermal grating component of the signal arises primarily from water vapor at the measurement location absorbing the pump laser radiation, while almost all other gases contribute mainly via electrostrictive grating formation. The dynamics of the grating growth and decay have been treated theoretically by Cummings et al. [19, 20], by Paul et al. [21], and Hemmerling and co-workers [22–26]. A useful introduction to the physics of laser-induced gratings is given in the textbook by Eichler et al. [27]. The technique has been amply demonstrated by Ewart and coworkers for applications in engines, and for a variety of gas measurement applications [28–33]. Recent studies [18] have indicated that it is also possible to correlate certain features in the signal to the water vapour concentrations of water in the mixture. In particular, a previous paper showed that measurements of temperature and relative water vapour concentration could be extracted from turbulent premixed methane-air flames in a gas turbine test facility [34, 35]. Recent advances have also extended LIGS into the femtosecond regime, enabling ultrafast, high-sensitivity diagnostics using multi-photon excitation. These developments have demonstrated improved temporal resolution, and enhanced signal-to-noise ratios, allowing operation under a wider set of conditions, and including non-resonant species [36–38].

In this work, LIGS is used to measure instantaneous local temperatures and water molar fractions in premixed swirlstabilized methane/hydrogen/air flames at 3 bar. Further, we extend a previously established model for the time signature of the LIGS signal to extract water vapour concentrations using features within the same signal. Measurements are conducted in the high-pressure, optically-accessible combustor facilities at the Cardiff Gas Turbine Research Centre (GTRC) using the Portable In-line LIGS for Optical Thermometry (PILOT) unit [34, 39, 40]. The effects of varying the volume fraction of methane/hydrogen blends at pressure for lean global equivalence ratios are investigated. Thermal and electrostrictive signatures are used to measure local temperatures and water molar fractions for 100% (0%), 70% (30%) and 40% (60%) methane (hydrogen) with global equivalence ratios of 0.600, 0.525 and 0.390, respectively. The PILOT unit is mounted on a motorized two-axis translation stage which enables scalar measurements at different radial and axial positions in the chamber. Previous reports have introduced the application of the LIGS technique to premixed methane/air flames in a realistic high-pressure gas turbine combustor [35]. The present work extends the previous measurements by detailing the procedure for extracting water vapour concentrations in both premixed methane and hydrogen flames.

This work is structured as follows: first, an overview of the experimental setup is provided, including the highpressure optical chamber (HPOC), burner configuration, and diagnostics instrumentation. The methodology section outlines the signal processing techniques used to extract frequency and intensity data from LIGS signals. Results for the local temperature spatial distributions are then presented, including frequency and temperature for three methane-hydrogen-air mixtures, and a discussion of the overlap with chemiluminescence measurements. A model for the time signature of the signals, and corresponding ratio of signal intensities between the second to first peaks are discussed, with a final model for the extraction of water vapour concentrations. The spatial distributions of water vapour concentrations are then presented. The overall results for temperature and water vapour are analysed based on flame structure, mixing behaviour. The study concludes with a discussion of the findings, the limitations of the technique, and recommendations for future work to improve the applicability of LIGS in combustion diagnostics.



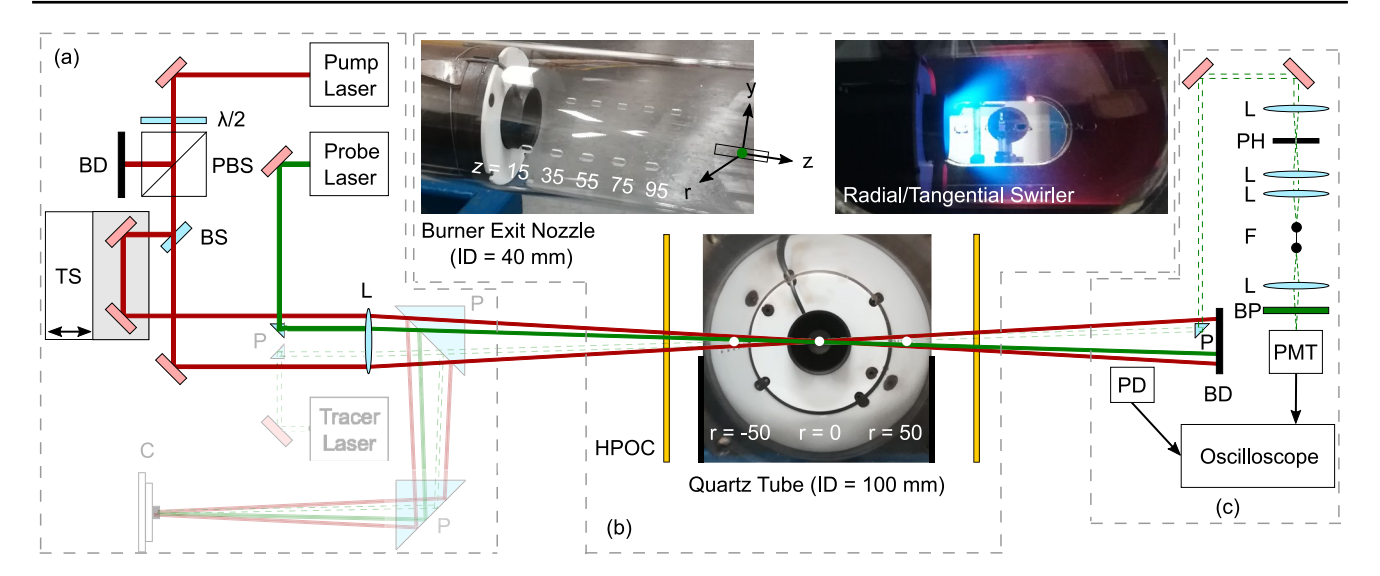


Fig. 1 Schematic of (**a**) the PILOT unit, showing the path of all three (pump, probe and tracer) beams, along with (**b**) a schematic of the modified quartz tube and (c) back-end collection optics. Pump: 1064 nm pulsed laser; Probe: 532 nm CW laser; Tracer: 532 nm DPSS Laser; λ

Table 1 Air, methane (CH₄), hydrogen (H₂) flow rates and corresponding volume fractions, and indicated corresponding equivalence ratio ϕ

#	Air	CH ₄	H_2	φ
	[g/s]	[g/s]	[g/s]	[-]
1	19.6	_	_	_
2	19.6	0.68 (100%)	- (0%)	0.600
3	22.0	0.60 (70%)	0.033 (30%)	0.525
4	28.5	0.47 (40%)	0.089 (60%)	0.390

2 Experimental methods

2.1 High pressure combustion rig and operating conditions

A high-pressure optical chamber (HPOC) houses the fully premixed methane-hydrogen-air swirl-stabilized burner. The swirling motion is imparted using a nine-blade axial swirler of geometric swirl number S=0.8. The HPOC has two outer one-inch thick rectangular Spectrosil windows (either side) which allow optical access. The flame itself is confined in a cylindrical quartz tube (3.5 mm thickness) with 100 mm inner diameter and 600 mm length containing five identical pairs of holes located at axial positions z = 15 mm, 35 mm, 55 mm, 75 mm and 95 mm (in Fig. 1) from the gas inlet plane. These slits are square $(4 \times 4 \text{ mm}^2)$, length × width) with rounded corners on the upstream and down stream ends (2 mm radius). These allow passage of the laser beams into the flame region with no distortion. Although there is no flow in the outer pressure chamber, air can be entrained into the flame tube or conversely products can leak out into the outer chamber at the nozzle exit.

/2: Half-Wave Plate; PBS: Polarisation Beam Splitter (for 1064 nm); TS: Translation Stage; BS: Beam Splitter (for 1064 nm); P: Prism; C: Camera; L: Lens; PD: Photodiode; BD: Beam Dump; PH: Pin Hole; F: Fiber; BP: Band-Pass Filter (for 532 nm); PMT: Photomultiplier Tube

The methane and hydrogen flow rates are controlled using Micro Motion ELITE Coriolis mass flow meters from pressurized gas cylinders. Air flow rates are controlled using a pair of Bronkhorst F203 mass flow controllers. A variable drive speed compressor, an air dryer, and two electric preheaters in series are employed to preheat and deliver air at a temperature of 500 ± 2 K. The combustion experiments are carried out under lean conditions, and the fuel flow rates are carefully regulated to maintain a constant power scaling (12.5 kW/1.1 bar) during combustion at 3.0 ± 0.1 bar absolute pressure. The mixture enters the chamber through the burner exit nozzle (d = 40 mm). The burner is first ignited at atmospheric pressure, and then the air and fuel mass flow rates are adjusted using a back pressure valve to achieve the desired operating condition. The resulting flame is relatively compact ($P \approx 34 \text{ kW}$ thermal power at 3 bar), with a conical shape anchored to the central lance which serves as a bluff body. A comprehensive description of the experimental rig and design is available in [41–43]. Table 1 shows the air, methane and hydrogen flow rates along with the corresponding global equivalence ratios for the three premixed cases used in this investigation.

2.2 PILOT system

Figure 1 shows the PILOT unit along with the perforated quartz tube and back-end collection optics. The PILOT unit [39] is used to perform tracer-free electrostrictive and thermal LIGS measurements, the latter enabled by the presence of water vapour in the HPOC. The system produces pump beams at 1064 nm (Nd:YAG Merion C laser from Quantel)



with repetition rates of up to 400 Hz and adjustable energies of up to 35 mJ per 10 ns pulse. The continuous probe beam at 532 nm (Verdi V-18 laser from Coherent) has an adjustable power of up to 18 W.

The spatial resolution of the measurement is determined by the geometry of the crossing pump beams, and their intersection with the probe beam, as described in [39]. The pump beams are focused using a 750 mm focal length lens, at a crossing angle of 3 degrees. The probe beam is delivered through the same lens at 0.8 degrees to the pump, leading to an overall intersection volume of approximately $0.3 \times 0.3 \times 6$ mm. The calculated grating spacing is determined to be 19.9 μ m.

The PILOT unit and collection optics are mounted on a 2-axis (axial (z) and radial (r)) motorised translation stage. This stage is not fixed directly to the HPOC, in order to minimise the effects of vibrations during rig operation. This also ensured that the collection optics could be translated in tandem with the beam delivery unit during the investigation. The motorized translation stage is used to collect LIGS signals across a wide range of axial (z = 15 mm, 35 mm, 55 mm, 75 mm, 95 mm) and radial ($r = \pm 0$ mm, 10 mm, 20 mm, 30 mm, 40 mm, 50 mm) positions in the combustor. Radial measurements were performed by directing the pump and probe beams through opposing slits in the quartz tube at each axial location, with the motorised translation stage moving the PILOT system to record signals at the specified radial positions along the horizontal plane. This enables measurements in the shear layers as well as the central and outer recirculation zones (in Fig. 4 for CRZ and ORZ, respectively).

A photomultiplier tube (Hamamatsu H10721-20) and a photodiode (Thorlabs DET210) are used to collect the signal and pump beams, respectively. The acquisition of the LIGS signal is triggered by the pump beam on a 4-channel Teledyne LeCroy 6104A High Definition oscilloscope (1 GHz Bandwidth, 4 Input Channels, 10 GS/s). The SNR of the LIGS signals is improved by introducing a spatial filter in the signal beam path (in Fig. 1)). This helped minimise

any reflected light from the HPOC windows and modified quartz tube.

3 Determination of temperature

3.1 Frequency and temperature calibration

The relationship between LIGS signal frequency f and temperature T is determined by the time it takes a pressure wave to pass through the fringe spacing Λ generated by the crossing laser beam, which depends only on the geometry of the laser beams and the pump laser wavelength. The measured frequency f is related to the speed of sound and thus temperature via $\lceil 10 \rceil$:

$$f = n_f \frac{v_s}{\Lambda} = \frac{n_f}{\Lambda} \sqrt{\frac{\gamma RT}{W}} \tag{1}$$

where v_s is the speed of sound, n_f takes the value of 1 or 2, depending on whether the signal arises from thermal or electrostrictive density changes. The speed of sound is given as the square root of the product of the ratio of specific heats, γ , the absolute temperature T, and the gas constant \mathcal{R}/W , where \mathcal{R} is the universal gas constant and W is the molecular weight. A reference temperature, T_A , in dry air is used to either determine the fringe spacing, or directly determine the temperature, T, via [34]:

$$T = T_{\rm A} \left(\frac{n_{f,\rm A}}{n_f} \frac{f}{f_{\rm A}}\right)^2 \frac{\gamma_{\rm A}}{\gamma} \frac{W}{W_{\rm A}} , \qquad (2)$$

where the subscript A refers to the reference conditions, which is here taken as the dry air temperature. In order to determine accurate temperatures we must also have insight into the reactant and product gas composition. Table 2 shows the calculated mixture values (calculated using Cantera 2.6.0 [44] and GRI Mech 3.0 [45] for the corresponding temperatures at the respective operating conditions) for the

Table 2 Reactant and expected adiabatic flame temperatures (AFTs), water molar fractions ($X_{\rm H_2O}$), molecular weights (W) and specific heat ratios (γ) for air (A), reactants (R) and products (P) for the four experimental conditions

#		AFT	$X_{ m H_2O}$	W	γ	$g = W/\gamma$
		[K]	[-]	[g/mol]	[-]	[g/mol]
1	A	285	0	28.85	1.400	20.61
	A	500	0	28.85	1.384	20.84
2	R	500	0	28.09	1.368	20.54
	P	1818	0.118	28.09	1.272	22.09
3	R	500	0	27.72	1.371	20.21
	P	1702	0.113	27.72	1.278	21.69
4	R	500	0	27.38	1.377	19.88
	P	1466	0.097	27.38	1.292	21.19



factor $g = W/\gamma$ for the reactant and product gas mixtures, which change by up to 6% over the conditions investigated.

In order to better account for the change between products, P, and reactants, R, in the premixed mixtures, it can be assumed that for all premixed flame properties, g varies linearly with the progress of reaction, as marked by product temperature, which is proportional to the square of the measured frequency. An interpolation based upon the square of the frequencies is used to determine all changes via

$$\frac{g - g_{\rm R}}{g_{\rm P} - g_{\rm R}} = \frac{f^2 - f_{\rm R}^2}{f_{\rm P}^2 - f_{\rm R}^2} \,. \tag{3}$$

The frequency can be determined with a resolution given by the signal frequency acquisition, $f_s=2.5$ Gs/s, and an effective record length of $N_s=20002$, leading to a frequency resolution of $\Delta f=f_s/N_s=0.125$ MHz for the FFT. The corresponding estimated resolution for temperature excepting the precision of the estimate of the factor g is therefore $\Delta T/T=2\Delta f/f$, which is of the order of 1/140 for typical electrostrictive frequencies of 35 MHz in room air, with $\Delta T\approx 2$ K. The final precision of the measurements is dependent on that of the dry air temperature determination as a baseline, which is estimated as $T_{\rm A}=285~\pm~2$ K.

3.2 Data processing

A detailed description of the signal processing steps carried out to determine the frequencies has been described previously [34], and is summarized here. A total of 1000 shots are collected at 11 different radial locations (-50 mm to 50 mm in 10 mm steps) and 5 different axial locations (15 mm, 35 mm, 55 mm, 75 mm and 95 mm away from the burner face). Each shot consisted of a voltage signal and time array of $N_s = 20002$ data points collected at $f_s = 2.5$ GS/s. Examples of signals and corresponding frequency content are shown in Fig. 2. Peak frequencies (between 20 and 90 MHz) and characteristic intensities are obtained from individual power spectra of voltage-time signals, with frequencies above and below 45 MHz classified as electrostrictive or thermal, respectively.

The procedure for determining frequency probability distributions (Fig 2(b)) follows our previous approach [34]. Each single-shot LIGS signal (PMT voltage vs time) is Fourier transformed to obtain its frequency spectrum. From each spectrum, only the dominant peak frequencies and their corresponding power magnitudes are retained. The peak frequency values are then binned into histograms (bin size 0.175 MHz, larger than the frequency resolution of f_s/N_s = 0.125 MHz), with the power magnitude used as a weight to reduce the impact of weak signals. Each histogram spans 400 bins between 20 and 90 MHz and is normalised by the count in the modal bin. In total, each histogram is formed

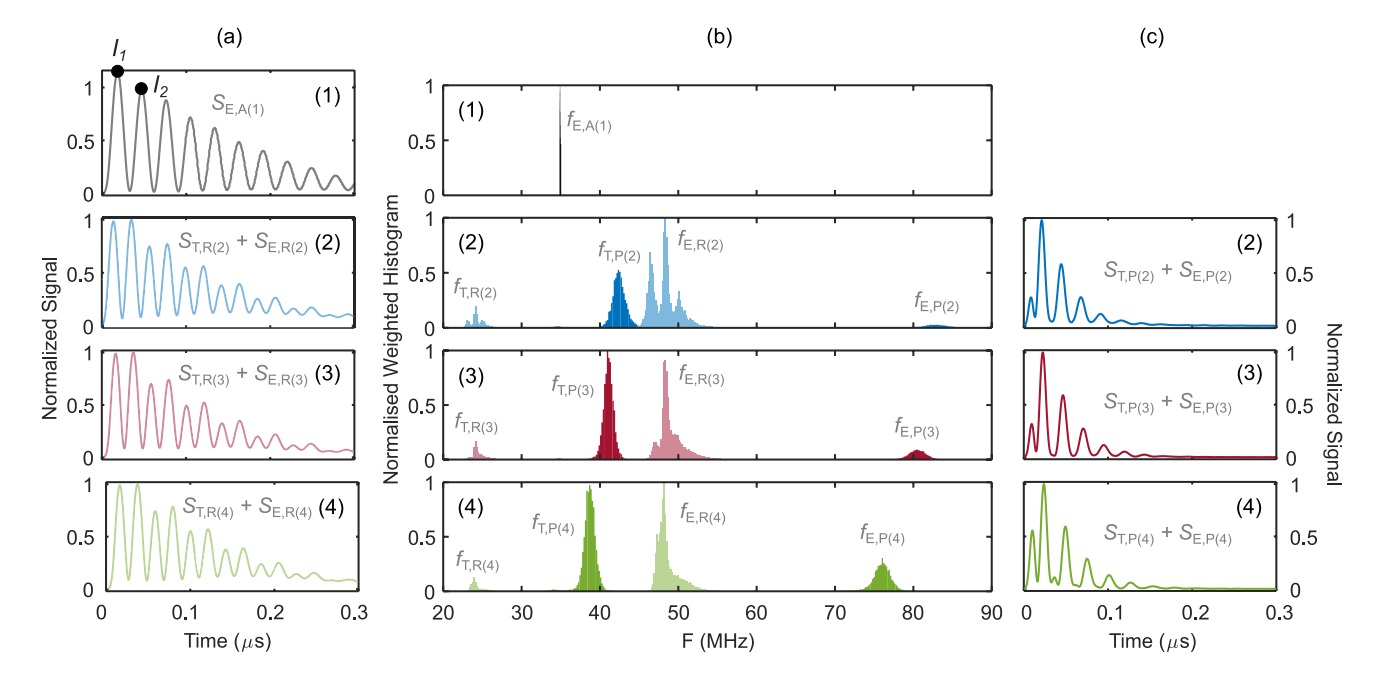


Fig. 2 Measured normalised LIGS signatures and frequencies for the four conditions row (1) dry air, row (2) 100% CH₄ row (3) 70% CH₄ and row (4) 40% CH₄. The measured average left (a) reactant and right (c) product normalised LIGS signatures as a function of time. Column (b) shows normalised weighted histograms for the four test conditions,

including data collected across all axial and radial measurement locations. Note both the reactant (R) and product (P) signatures contain frequencies of both thermal (T) and electrostriction (E). The labels I_1 and I_2 represent the first and second peak magnitudes, respectively



from 55,000 LIGS signatures (1,000 at each of 11 radial and 5 axial locations).

3.3 Analysis of time and frequency domain signal characteristics

The LIGS temporal signal is characterised by the growth and decay of the induced thermal and electrostrictive gratings. Signals obtained in mixtures of different composition and density exhibit different characteristics due to their specific blend of thermal and electrostrictive response. For all three fuel blends and 55 regions (consisting of 1000 shots at each of the 11 radial locations at each 5 axial locations), three different characteristic signals are identified. Examples of the LIGS signature temporal behaviour, typical for air, reactants and products are shown in Fig. 2 (a) and (c) for the four cases enumerated in Table 1. Each voltage signal is normalised to the second (and often highest) peak.

Figure 2 shows normalised LIGS signals for reactants (column (a)), and products (column (c)), for dry air (row 1), and the three operating conditions (rows 2–4). The middle column (b) shows the overlaid frequency histograms for the four cases described in Table 1. The dry air signal (Fig. 2 (a) row (1)), is purely electrostrictive, with several oscillations over a time duration of 350 ns. The labels I_1 and I_2 represent the first and second peak magnitudes, respectively. For a purely electrostrictive signature, the first peak is higher than the second.

The reactant time signals (Fig. 2 (a) (2, 3, 4)), are predominately electrostrictive with a small thermal contribution as a result of ambient water in air and water recirculating from the products, formed during combustion. In this intermediate regime, between the electrostrictive and thermal limits, the even-numbered peaks are enhanced, and the odd-numbered peaks are not enhanced [23]. All three reactant spectra under investigation look very similar to that of dry air but with a shorter acoustic transit time of approximately 260 ns in each case owing to the increased temperature. The maximum molar fraction of water at atmospheric conditions (300 K and 1 bar) in the incoming air to the compressor is the saturation value corresponding to 2% by volume.

The product time traces (Fig. 2 (c) (2, 3, 4)), are dominated by the thermal contribution to the signals instead. This is shown by the presence of an electrostrictive peak which appears as a prompt signal after the laser pulse, followed by a second much higher peak delayed by a time corresponding to half of the period of the thermal acoustic oscillations. All three product signals under investigation have a strong thermal contribution with decay durations limited by molecular diffusion and acoustic packet loss. The presence or absence of the second harmonic depends on the decay time of the electrostrictive oscillations. In some cases, such as

Fig. 2 (c) (4) several subsidiary maxima due to electrostriction are barely visible, whilst in product (c)(2-3), electrostrictive contributions are limited to the first peak only.

We now turn to the central panel, column (b) in Fig. 2 for the four cases described in Table 1. The spectra represent data collected from all locations rather than at a single position to allow a clearer identification of the characteristic frequencies for the corresponding thermal and electrostrictive values for each fuel blend. Each histogram is normalised to the modal bin within each distribution. The lighter and darker coloured frequency modes correspond to the reactant (R) and product (P) temporal signatures shown in Fig. 2 (a) and (c), respectively. Note that both the reactant and product signatures contain frequencies of both thermal (T) and electrostriction (E) of relative strengths corresponding to the dominant (higher or lower energy) mechanism for each

Figure 2 (b) (1) shows the distribution of electrostrictive frequencies associated with dry air at atmospheric pressure and a temperature value of $T_A=285\pm2$ K. For dry air the electrostrictive frequencies correspond to a value of 35.1 ± 0.2 MHz with a narrow standard deviation given the minimal shot-to-shot variations of temperature and air composition in the probe volume. The measured standard deviation is only slightly higher than the nominal frequency resolution of 0.125 MHz, so the room temperature was clearly stable, and the measurement precision was similar to the measurement resolution. We note that the precision (STD/Mean) is equal to 0.6% for the measured electrostrictive frequencies.

Figures 2 (b) (2), (3) and (4) show the distributions of thermal and electrostrictive frequencies associated with the reactant and product species for the 100% CH₄, 70% CH₄, and 40% CH₄, fuel blends respectively. Mean and standard deviation of the (darker) shapes associated with thermal frequencies measured from product gases are 42.5 ± 0.8 MHz, 41.1 ± 0.6 MHz and 38.7 ± 0.6 MHz, for the three operating conditions, respectively (darker colours, marked $f_{T,P}$). We note that the precision (STD/Mean) is equal to 1.9%, 1.5% and 1.6% for the measured product thermal frequencies, respectively. The corresponding mean frequency from electrostrictive in product gases appears as a value approximately twice that of the thermal frequency associated with each fuel blend (darker colours, marked $f_{E,P}$). The mean thermal and electrostrictive frequency values decrease with methane percentage because of the increase in excess air resulting from the lower equivalence ratio (0.6 down to 0.375), corresponding to lower AFTs (1818 K down to 1466 K, in Table 2). The ratio of thermal to electrostrictive frequency content also decreases with a decrease in frequency, as the thermal contribution fraction to the overall spectrum decreases for the lower AFT. This is shown



by the emergence of extra electrostrictive peaks such as in Fig. 2 (c) (4).

The electrostrictive peaks corresponding to the reactants (lighter colours, marked $f_{\rm E,R}$), appear between 46 and 50 MHz. For the 100% CH₄ fuel blend (b (2)), three distinct mean electrostrictive reactant frequency peaks are measured at 46.4 \pm 0.4 MHz, 48.3 \pm 0.4 MHz and 50.1 \pm 0.4 MHz. The different values are associated with different regions in the flame containing different fractions of product relative to reactant, as discussed in section 3.6. The corresponding peaks associated with thermal reactant frequencies appear at a location corresponding to half the value of the electrostrictive reactant frequency associated with each mean (very weak peaks at about 24 MHz). For the case of 70% CH₄ and 40% CH₄ fuel blends, a wide distribution is also measured, corresponding to different locations, but with frequencies that are similar to (b (2)). We note that the precision (STD/ Mean) is equal to 0.8% for all measured electrostrictive reactant frequencies. The thermal peaks originating from the reactants are relatively short compared to the electrostrictive reactant peaks because of the relatively low water content in the reactant gas flow.

3.4 Calculated temperatures

The frequencies determined in section 3.3 are translated into temperatures using the procedure discussed in section 3.1. Figure 3 shows the calculated temperature distributions for 1000 shots at each of the 55 locations for the three premixed cases described in Fig. 2. The height of each bin is normalised by the modal bin height peak magnitude in the histogram. The measured means and standard deviations

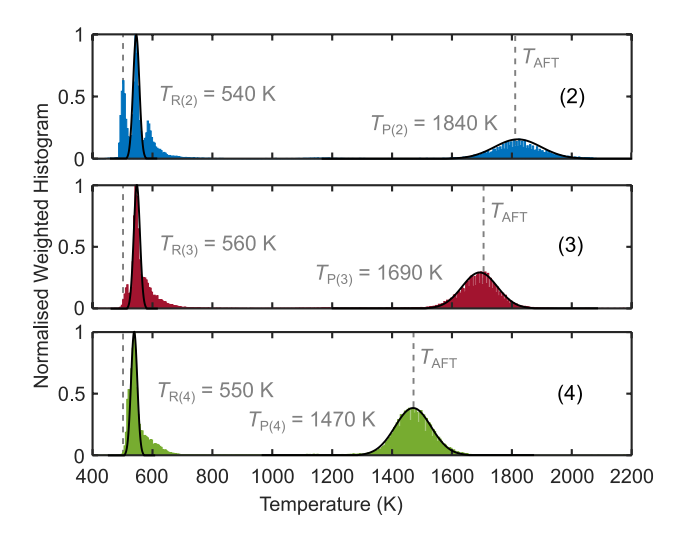


Fig. 3 Temperature histograms derived from the LIGS signals shown in Fig. 2. The plots contain the values for (2) 100% CH₄ (blue), (3) 70% CH₄ (red) and (4) 40% CH₄ (green). The grey vertical dotted lines are the thermocouple-measured preheat temperature (500 K) and computed adiabatic flame temperatures for each case

are determined from the black solid Gaussian fits to each plot. Figure 3 (2)-(4) show calculated mean and standard deviations for the measured reactant and product temperatures of $T_{\rm R(2)}=540\pm40$ K, $T_{\rm R(3)}=560\pm40$ K, $T_{\rm R(4)}=550\pm40$ K and $T_{\rm P(2)}=1840\pm80$ K, $T_{\rm P(3)}=1690\pm60$ K, $T_{\rm P(4)}=1470\pm60$ K for (2) 100% CH₄, (3) 70% CH₄ and (4) 40% CH₄, respectively.

The calculated coefficients of variation on temperature are 4.3%, 3.6% and 4.0%. The mean product temperatures are in excellent agreement with the calculated adiabatic flame temperatures of 1818 K, 1702 K and 1466 K (described in Table 2). The width of the product gas temperature distribution is significantly larger than the technique's underlying frequency resolution (for 100% CH₄ $\Delta T \approx$ 11 K and a precision of 0.6%), and represents the true deviation, which could arise from small fluctuations in global and local equivalence ratio or fuel/air delivery about the mean.

The histograms of reactant temperature data are more complex to interpret. For the 100% CH₄ (2) case, three distinct peaks are observed. The central peak is consistent for all three fuel blends and corresponds to the 6 mm measurement volume averaging temperatures close to the walls, capturing regions with mixing between reactants and air outside the quartz tube. The higher temperature peak in Fig. 3 corresponds to the ORZ, where temperatures are slightly elevated due to mixing of product gases with air entering through the holes in the quartz cylinder. This peak becomes cooler and merges with the central peak from (2) to (3) to (4), consistent with the decreasing AFT as methane content is reduced. The lower temperature peak increases with hydrogen content and is interpreted as the temperature of reactants near the burner surface, potentially influenced by heat transfer to the burner or expansion in the flow. These reactant temperatures are slightly higher than the thermocouple-measured inlet air temperature of 500 K. Filtering the data by measurement location will help clarify the origin of the three distinct peaks. The differences across regions reflect varying degrees of mixing with products, as further highlighted in section 3.6.

3.5 Chemiluminescence maps

The chemiluminescence setup used in the study has been described previously [46]. Chemiluminescence images of the excited hydroxyl (OH*) radical at a wavelength of 310 nm are used as a marker of the location of localized heat release rate. A high-speed camera (Phantom v1212 CMOS camera) coupled to a high-speed image intensifier (SIL40HG50) and a UV lens (78 mm focal length, F-stop = f/11), together with narrow band pass filters (center wavelength of 315 nm) is used to capture the OH* signals.



Note that the chemiluminescence images (in Fig 4) of the premixed operating conditions are not taken at the same time as the data obtained by the LIGS PILOT system, as the experiments are repeated without the laser system in place. For the images taken, the setup allowed for a resolution of approximately 5 pixels mm⁻¹, with the focus of the image plane aligned to the center of the burner exit nozzle. The optical access of the staged combustor within the HPOC permitted respective view fields of 100 mm in the radial and 100 mm in the axial direction. For each of the experimental conditions the chemiluminescence results comprise of 2000 images recorded at a rate of 4 kHz (sample time = 0.5 s). An intensifier gain value of 3 and a gate setting of 10 μ s is used. After a background correction is applied, an averaged image is produced, from which normalised planar representations OH* chemiluminescence intensity distributions are generated using a modified open-access Abel inversion algorithm [47], assuming cylindrical symmetry.

3.6 Temperature maps

Figure 5 shows temperatures obtained from the frequency measurements, as a function of radial location at the five axial locations of z=15, 35, 55, 75 and 95 mm from the burner edge. Only the positive radial locations are shown, as the results are symmetrical about about zero radius. The symbol colour intensity indicates the magnitude of the individual power spectrum intensities. The dotted horizontal grey lines correspond to the equilibrium adiabatic flame (top) and thermocouple-measured inlet (bottom)

temperatures for each combustion case. The vertical grey solid bands indicate the location of the cylindrical quartz tube. The solid regions highlight the approximate location of the flame brush, which is located in different regions for each fuel blend and measured separately using chemiluminescence (in section 3.5). A reminder that small slots in the flame tube wall are provided for laser beam passage without damage to the tube and this may allow some leakage of air, reactants or products across the quartz tube boundary. The overlap of the laser beams defines the spatial resolution of the LIGS sample volume, which is estimated as 6 mm in length, and of the order of the beam diameter, 0.3 mm in the other directions [39]. Measurements are therefore taken radially every 10 mm.

In Figure 5 the temperature profiles are shown for the 100% CH₄ (blue), 70% CH₄ (red) and 40% CH₄ (green) cases at the various radial and axial locations from the burner face. The lowest temperatures are just above the inlet heater temperature of 500 K. The highest temperatures agree very well with the estimated adiabatic flame temperatures based on the reactant mixture composition. Considering temperature evolution as a function of radial and axial position, we observe a few different characteristics depending on the case. The regions where temperatures transition from reactant to product largely overlaps with the observed flame brush location based on previous studies of chemiluminescence, as marked by the regions. However, there are a few deviations. We expect some mixing between reactants and products in the ORZ. In case 2 (column (2)) for 100% CH₄, measured temperatures remain relatively constant

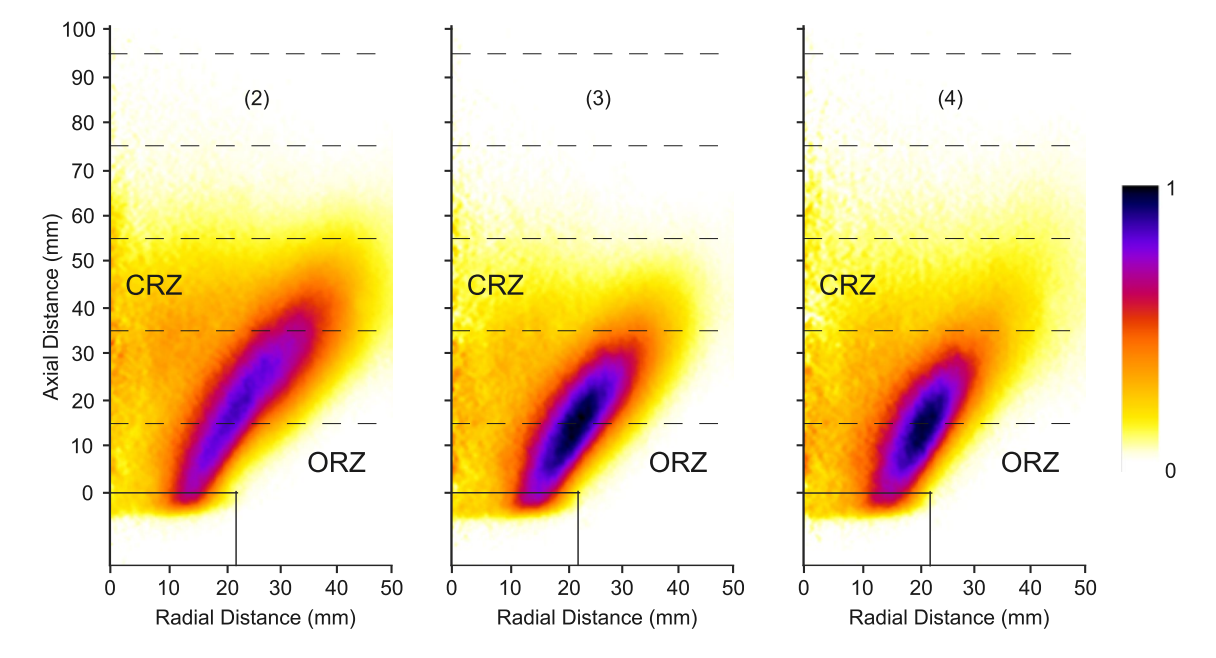


Fig. 4 Abel-transformed OH* chemiluminescence images as a function of axial and radial distances. The three columns indicate the three combustion cases, (2) 100% CH₄, (3) 70% CH₄ and (4) 40%

CH₄, respectively. The black dotted lines correspond to the locations of LIGS temperature and water concentration measurements. The solid black box corresponds to the injector location



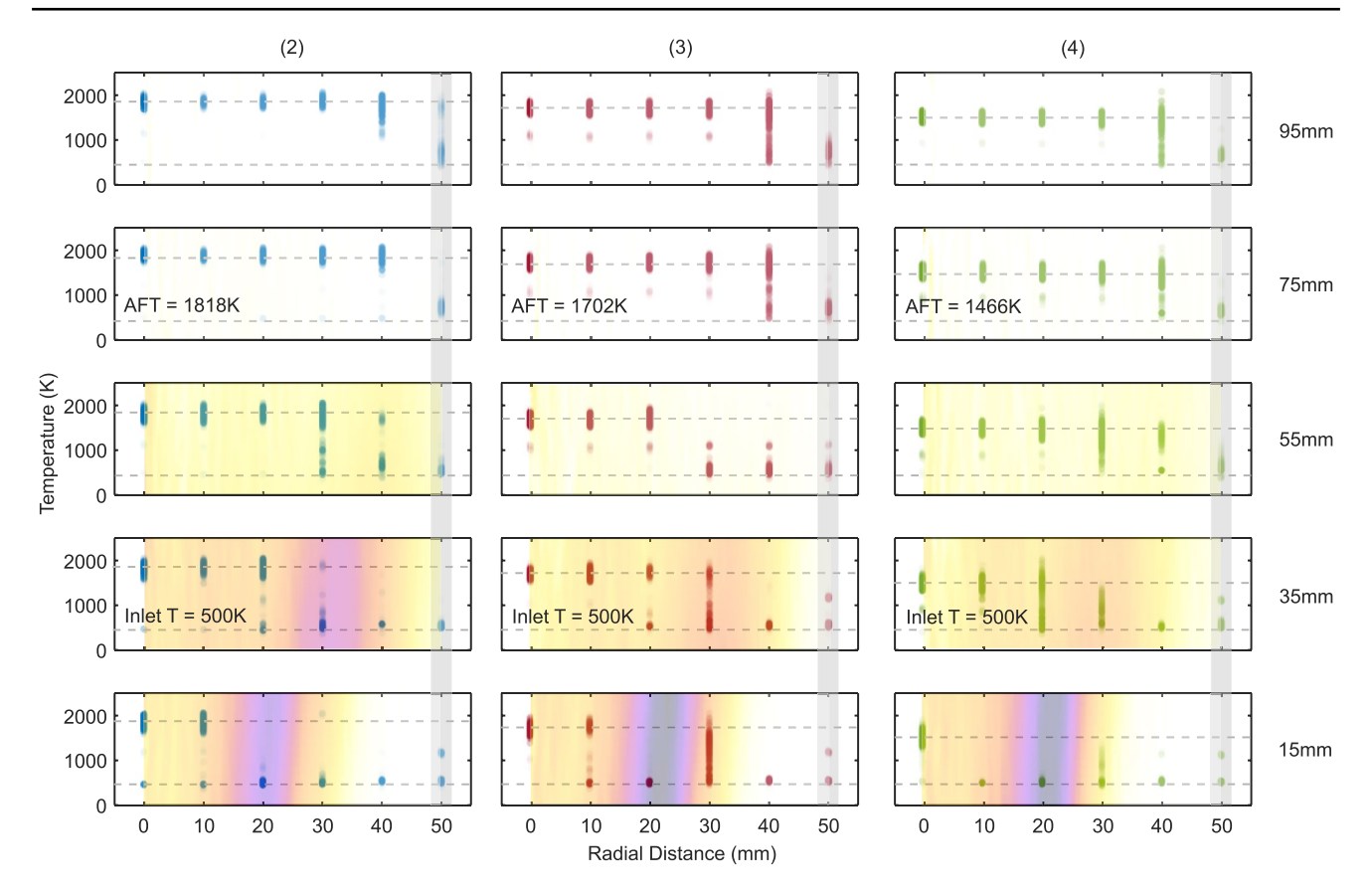


Fig. 5 Temperature as a function of radial locations at axial distances of 15 mm, 35 mm, 55 mm, 75 mm and 95 mm from the burner edge. The three columns indicate the three combustion cases, (2) 100% CH₄ (blue), (3) 70% CH₄ (red) and (4) 40% CH₄ (green), respectively. The intensity indicates the magnitude of the individual power spec-

trum intensities. The grey dotted lines correspond to the equilibrium adiabatic flame and inlet temperatures for each combustion case. The grey solid regions highlight the location of the cylindrical quartz tube. The chemiluminescence images correspond to the flame brush regions shown in Fig 4.

down stream. This suggests that the flames simply exhaust down stream, with minimal recirculation of burned gases.

For the 70% $\rm CH_4$ case (column (3)) there appears to be a band around radius 30-40 mm in which both products and reactants are present in the ORZ beyond the flame brush, suggesting that there is a recirculation zone of products, reactants and products mixing with reactants. Evidence of mixing is also present in the down stream region beyond 75 mm. Finally, for the 40% $\rm CH_4$ (4) in which the flames are much shorter, there is a region around r=30 mm for axial positions 15 mm and 35 mm, where high temperatures are detected, indicating recirculation, as well as regions down stream of the flame brush in which mixed temperatures are found, suggesting entrainment of reactants.

The highest measured temperatures appear near the edge of the inner recirculation zone (IRZ) of the swirling flames, with measured values of 1840 \pm 80 K, 1690 \pm 60 K and 1470 \pm 60 K for the 100% CH₄ (blue), 70% CH₄ (red) and 40% CH₄ (green) cases. This compares to calculated adiabatic flame temperatures of 1818 K, 1702 K and 1466 K for equivalence ratios of 0.600, 0.525 and 0.390, and a

reactant inlet temperature of 500 K and pressure of 3 bar (see Table 2). The temperatures at the centerline are slightly lower by up to 100 K. This may be a result of the entrainment of unburned reactants from down stream regions via the extended inner recirculation zone (IRZ).

4 Obtaining water vapour concentration from LIGS signals

Previous LIGS experiments in the product zones of laminar flames have shown that there is a direct correlation between the ratio of the second to the first peak intensities, $R = I_2/I_1$ (see Fig. 2 (1) (a)) and the molar fraction of water vapour in the products [18]. The suggested explanation is that the intensity of the second peak is proportional to the fraction of energy absorbed by the water vapour present, whilst the first peak is purely electrostrictive. In this section, we discuss the theory of a generated LIGS signal, and apply it to the present results. Then, we discuss how the ratio R is expected to vary with equivalence ratio, and compare the



predicted overall results to the corresponding experimental values. Finally, we use the ratio of intensities to determine the instantaneous molar fraction of water vapour.

4.1 Expanding the model for LIGS signals

A theory for the time evolution of the LIGS signal has been proposed by previous investigators [23, 48, 49]. The model describes how the spatially-modulated density perturbation that underlies a laser-induced grating is generated by two different processes, namely electrostriction and resonant absorption. Note that a spatially stationary (yet time varying) density perturbation may coexist with a density perturbation generated by the transit of acoustic wave packets. The acoustic component is only significant in the case that the initial density perturbation happens on a timescale that is rapid compared to the grating lifetime. Different time scales govern the three energy transfer modes, denoted as 1) electrostriction (e), 2) instantaneous energy deposition associated with absorption of light and thermalisation via a rotational-translational (RT) transition (i), and 3) a slower (but still fast) rate of deposition associated with energy transfer from the excited states as they thermalise through vibrational-translational (VT) energy transfers (f).

The theory can be summarized in the following equations in terms of the grating scattering efficiency, $\eta(t)$, defined as the ratio of the scattered light intensity of the read-out probe laser, I_s , to the incoming probe laser intensity, I_0 , as a function of time, t, for a laser pulse exhibiting a Gaussian temporal profile [22].

$$\begin{split} &\eta(t) = \frac{I_{\rm s}}{I_0} \\ &= \left\{ M_{\rm e} {\rm Im} \left(\exp{(B)} \left(1 + {\rm erf} \left(\frac{\sqrt{2}}{\tau} \left(t - A \right) \right) \right) \right) \right. \\ &+ \left. M_{\rm i} \cos(\omega t) \exp{\left(- \left(\frac{t}{\tau_{\rm tr}} \right)^2 - \frac{t}{\tau_{\rm a}} \right) - M_{\rm i} \exp{\left(- \frac{t}{\tau_{\rm th}} \right)} \right. \\ &+ \left. M_{\rm f} \left(\frac{k_{\rm f}}{A_{\rm f}^2 + k_{\rm f}^2} \right) \sin{(\omega t)} \exp{\left(- \left(\frac{t}{\tau_{\rm tr}} \right)^2 - \frac{t}{\tau_{\rm a}} \right)} \right. \\ &- \left. M_{\rm f} \frac{\left(\exp{\left(- \frac{t}{\tau_{\rm th}} \right)} - \exp{\left(- \frac{t}{\tau_{\rm f}} \right)} \right)}{\left(1 - \frac{\tau_{\rm f}}{\tau_{\rm th}} \right)} - M_{\rm f} \left(\frac{A_{\rm f}}{A_{\rm f}^2 + k_{\rm f}^2} \right) \exp{\left(- \frac{t}{\tau_{\rm f}} \right)} \right\}^2 \end{split}$$

where

$$A = \tau_{\rm c} + \frac{\tau^2}{4} \left(\frac{1}{\tau_{\rm a}} + \frac{1}{\tau_{\rm tr}} - i\omega \right) , \qquad (5)$$

$$B = \frac{\tau^2}{8} \left(\frac{1}{\tau_{\rm a}} + \frac{1}{\tau_{\rm tr}} - i\omega \right)^2 - \left(\frac{1}{\tau_{\rm a}} + \frac{1}{\tau_{\rm tr}} - i\omega \right) (t - \tau_{\rm c}) , \qquad (6)$$

and τ and τ_c are the duration and coherence of the excitation pulses, respectively, and the error function, erf, has its normal definition. The other terms in eqs. 4, 5 and 6 are explained as follows. The angular frequency value

 $\omega=\frac{2\pi}{\Lambda}v_s=2\pi f$ arises from the interaction of a stationary and acoustic modulation to the density. The amplitudes $M_{\rm e}$, $M_{\rm i}$ and $M_{\rm f}$ represent the effects of electrostriction, instantaneous and fast energy deposition, respectively [50, 51]. They are described by the following expressions:

$$M_{\rm e} = \frac{\pi L}{\lambda_{\rm pr}} \left(\frac{\partial n_{\rm p}}{\partial \rho} \right)_T \Delta \rho_e = \frac{\pi L}{\lambda_{\rm pr}} (k\rho)^2 \left(\frac{2E}{cs} \frac{\omega}{\rho v_s^2} \right) \tag{7}$$

$$M_{\rm i} = \frac{\pi L}{\lambda_{\rm pr}} \left(\frac{\partial n_{\rm p}}{\partial \rho} \right)_T \frac{\beta_{\rm p} \Delta \epsilon_{\rm RT}}{c_{\rm p}} N_{\rm u} = \frac{\pi L}{\lambda_{\rm pr}} (k \rho) \left(\frac{2E}{\rho c_{\rm p} T} \frac{\bar{a}}{s} \right) \frac{\Delta \epsilon_{\rm RT}}{h \nu_{\rm p}}$$
(8)

$$M_{\rm f} = \frac{\pi L}{\lambda_{\rm pr}} \left(\frac{\partial n_{\rm p}}{\partial \rho} \right)_T \frac{\beta_{\rm p} \Delta \epsilon_{\rm VT}}{c_{\rm p}} \frac{\tau_{\rm f}}{\tau_{\rm R}} N_{\rm u} = M_{\rm i} \frac{\Delta \epsilon_{\rm VT}}{\Delta \epsilon_{\rm RT}} \frac{\tau_{\rm f}}{\tau_{\rm R}}$$
(9)

In all cases, the amplitudes are proportional to the diffraction efficiency at the Bragg angle, $\frac{\pi L}{\lambda_{\rm pr}}$, which accounts for the fraction of light diffracted by the length of the probe volume, L, at wavelength λ_{pr} . The factor is multiplied by the sensitivity of the index of refraction $n_{\rm D}$ to the equilibrium mass density ρ , multiplied by the magnitude of the density fluctuation $\Delta \rho$ for the particular process. The magnitude of $\Delta \rho$ depends on the assumptions made regarding the energy transfer process, and whether it is electrostrictive or thermal. For all terms, the assumption is made that $\left(\frac{\partial n_{\rm p}}{\partial \rho}\right)_T = \frac{(n_{\rm p}-1)}{\rho} = k$, assumed to be a constant for each mixture and equal to $\frac{n_{\mathrm{p}}-1}{\rho}=k=\sum_{i}k_{i}Y_{i},$ where k_{i} and Y_{i} are the Gladstone-Dale constant and mass fraction for each species, respectively [52–54]. The factor $\beta_p = \left(\frac{\partial \rho}{\partial T}\right)_{-} = \frac{1}{T}$ is the expansion coefficient at constant pressure, and $N_{\rm u}$ is the number concentration of molecules at the corresponding upper state.

The resulting expression for the electrostrictive term $M_{\rm e}$ involves the non-dimensional term $(k\rho)^2$, representing the sensitivity of the index of refraction to the density change produced by the electric field, multiplied by the term $\left(\frac{2E}{cs}\right)$ as the energy input, 2E, per unit swept volume and time, (cs) as the product of speed of light c and s is the cross sectional area of the interaction volume along the pump beam path, divided by the term $\left(\frac{\rho v_s^2}{\omega}\right)$, representing the product of the acoustic energy per unit volume and acoustic time [23].

The second term, $M_{\rm i}$, is associated with the instantaneous energy transfer via absorption/release via the higher rovibrational energy state, $\Delta\epsilon_{\rm RT}$, and the population density of excited states, $N_{\rm e}$. The latter is expressed as $N_{\rm e}=\frac{2E\lambda_{\rm p}}{hcs}\bar{a}$ where \bar{a} is the density-dependent absorption coefficient (in units of reciprocal length), $\lambda_{\rm p}$ is the pump wavelength for each absorption line. The final term is proportional to the term $(k\rho)$ representing the sensitivity of index of refraction to density change, multiplied by the pulse energy absorbed



per unit volume divided by the total enthalpy of the mixture per unit probe volume $\left(\frac{2Ea_n}{s}\right)$, divided by the total enthalpy of the gas per unit volume, $(\rho c_p T)$, where c_p is the specific heat capacity at constant pressure. The quantity is multiplied by the ratio of the energy gap for the rotational-translational transition $\Delta \epsilon_{\rm RT}$ to the pump photon energy, $h\nu_{\rm p}$, where h is Planck's constant and $\nu_{\rm p}$ the frequency of the pump beam.

Finally, the amplitude $M_{\rm f}$ is associated with a slower energy transfer mode, and is assumed as in the original work [23] to be equal to the amplitude $M_{\rm i}$, but scaled to the corresponding energy level difference, and by the ratio of corresponding relaxation times.

The time constants due to thermal diffusion, $\tau_{\rm th}$, acoustic damping, $\tau_{\rm a}$, acoustic transit, $\tau_{\rm tr}$, molecular mass diffusion, $\tau_{\rm d}$ and collisional relaxation, $\tau_{\rm f}$ are given by

$$\tau_{\rm th} = \frac{1}{\alpha} \left(\frac{\Lambda}{2\pi} \right)^2 = \frac{G}{\alpha} = \frac{G \,\mathrm{Pr}}{\nu} ,$$
(10)

$$\tau_{\rm a} = 2\left(\frac{\Lambda}{2\pi}\right)^2 \left(\frac{4}{3}\nu + (\gamma - 1)\alpha\right)^{-1} = 2\frac{G}{\alpha}\left(\frac{4}{3{\rm Pr}} + (\gamma - 1)\right)^{-1} \tag{11}$$

$$\tau_{\rm tr} = \frac{w_0}{\sqrt{2}v_s} \tag{12}$$

$$\tau_{\rm d} = \left(\frac{\Lambda}{2\pi}\right)^2 \frac{1}{D} \approx \frac{G}{\alpha}$$
(13)

$$\tau_{\rm f} = \frac{1}{\frac{1}{T_{\rm VT}} + \frac{1}{\tau_{\rm d}}} \,\,\,(14)$$

Here the thermal diffusion time $\tau_{\rm th}$ is proportional to the ratio $G=\left(\frac{\Lambda}{2\pi}\right)^2$, the squared fringe spacing distance, Λ , to the thermal diffusivity, $\alpha=\frac{\nu}{\Pr}$, where ν is the kinematic viscosity, both connected by the Prandtl number, Pr.

The molecular mass diffusion time, τ_d , is assumed to be similar to that of the thermal time. The acoustic damping time $\tau_{\rm a}$ is proportional to the thermal time but for a constant depending on Pr and the ratio of specific heats. The acoustic transit time $\tau_{\rm tr}$ is the time for a wave to traverse across the pump beam width $w_0 = \frac{2\lambda_{\rm p}F}{\pi d}$, where d is the pump beam diameter at the lens with focal length F.

The overall fast rate of relaxation $1/\tau_{\rm f}$ is taken as the sum of the mass diffusion relaxation rate and the relaxation rate for the vibrational-translational transfer, $1/\tau_{\rm VT}$. The latter rate is assumed to be a first order function of number density, $1/\tau_{\rm VT} = k_{\rm VT}N_0$ [55, 56]. There are many different routes by which excited water molecules can release energy, and $\tau_{\rm VT}$ should describe the overall relaxation time for the particular process. The value for $k_{\rm VT}$ is obtained from previous work, and is further described in section 4.4 [50,

56–58]. The remaining parameters in Eq. 4 are defined as: $k_{\rm f}=\omega \tau_{\rm f}$ and $A_{\rm f}=1-\frac{\tau_{\rm f}}{\tau}$.

The temporal signatures of thermal and electrostrictive gratings are quite different [21]. The electrostrictive signal rises promptly, while the thermal signal exhibits an induction period. Both mechanisms produce density perturbations that oscillate at the same frequency. However, the electrostriction signal arises through adiabatic compression; thus the density fluctuates about the mean; conversely, the thermal source involves net energy absorption, leading to a net increase in temperature and decrease in mean density, with a density oscillation about the lower mean value.

The shape of the resulting LIGS signature described by Eq. 4 is such that the ratio of the second to the first peak intensity depends on the ratios of the absorption to electrostrictive constants, along with the average energy contributions from translational, rotational, and (if thermally accessible) vibrational energies. We next define the following scaling ratios in the description of the overall intensities:

$$r_{\rm ie} = \frac{M_{\rm i}}{M_{\rm e}} = (\gamma - 1) \frac{1}{k\rho} \frac{\Delta \epsilon_{\rm RT}}{h\nu_p} \frac{c\bar{a}}{\omega}$$
 (15)

$$r_{\rm fe} = \frac{M_{\rm f}}{M_{\rm e}} = (\gamma - 1) \frac{1}{k\rho} \frac{\Delta \epsilon_{\rm VT}}{h\nu_p} \frac{\tau_{\rm f}}{\tau_{\rm VT}} \frac{c\bar{a}}{\omega}$$
 (16)

The sign of $r_{\rm ie}$ is related to the direction of the corresponding energy exchange that is defined by the rovibronic transition used for excitation. The heat exchanged per excited molecule, $\Delta\epsilon_{\rm RT}$, is positive or negative when the energy is released or absorbed into the medium, respectively. The sign of $r_{\rm fe}$ is positive and scales with the ratio of the upper number density to total number density. Section 4.2 discusses how the values of $\Delta\epsilon_{\rm RT}$, $\Delta\epsilon_{\rm VT}$ and \bar{a} are obtained, and section 4.4 the method to determine $\tau_{\rm VT}$.

4.2 Absorption properties of H₂O molecules

The pump excitation wavelength used is $\lambda_p=1064$ nm ($\nu_p=9398.50\pm0.70~{\rm cm^{-1}}$). A number of rovibrational transitions are covered in this range, between 9397.8 and 9399.2 cm⁻¹. We therefore adopt a mean value of the density-dependent absorption coefficient, \bar{a} , over the range of wavelengths with the value calculated using the HITEMP database via SpectraPlot [59]. Figure 6 (a) shows the simulated water absorption, a, spectrum near 1064 nm at 3 bar as a function of wavenumber for several temperature and water vapour molar fractions. The simulation is performed using SpectraPlot and the NIST ASD database [59]. Figure 6 (b) shows a polynomial fit to the absorption coefficient values, \bar{a} , across this spectral range as a function of temperature and water vapour molar fraction for each experimental



201 Page 12 of 19 L. Weller et al.

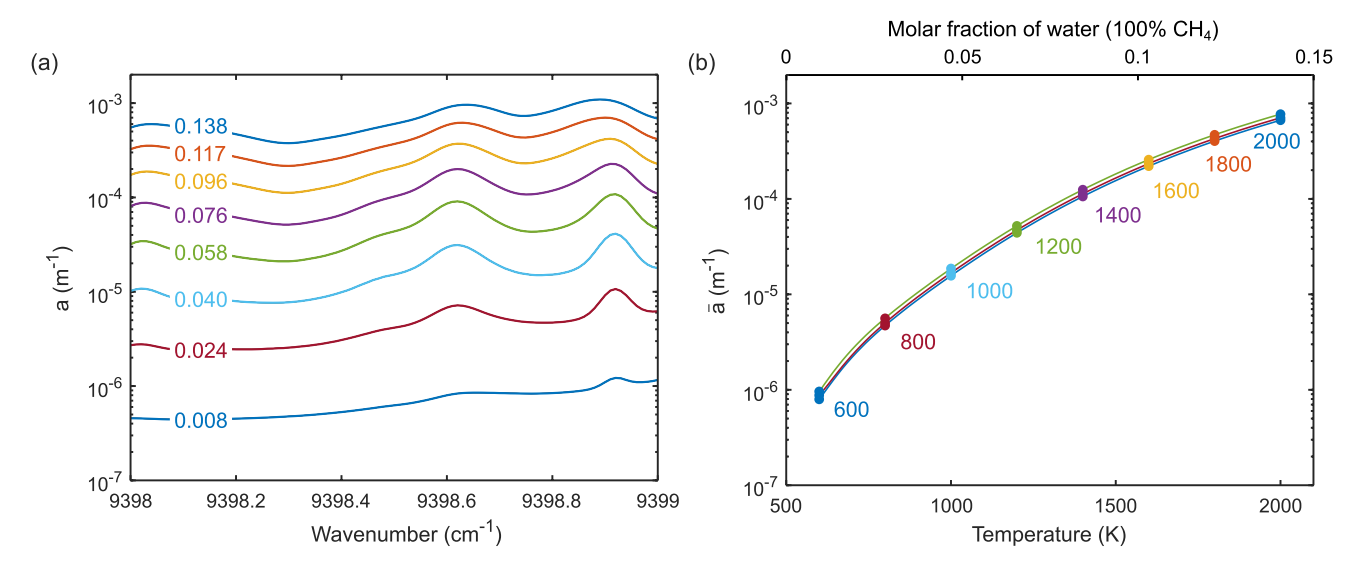


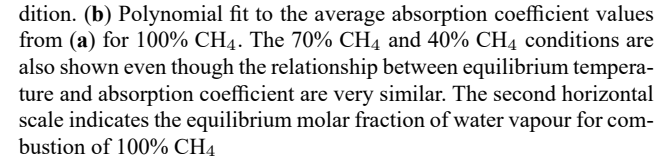
Fig. 6 (a) Simulated water absorbance spectrum at different temperatures and water molar fractions near 1064 nm at 3 bar for 100% CH $_4$. Line colours represent molar fraction values of 0.008 (600), 0.024 (800), 0.040 (1000), 0.058 (1200), 0.076 (1400), 0.096 (1600), 0.117 (1800) and 0.138 (2000). These values are calculated using Cantera 2.6.0 [44] and GRI Mech 3.0 [45] at the 100% CH $_4$ operating con-

condition. Temperature and water molar fraction are related by an equilibrium relationship, calculated using Cantera 2.6.0 [44] and GRI Mech 3.0 [45] for each condition. The connection is discussed further in section 4.4.

In order to determine the magnitude of the average energies exchanged per input photon for instantaneous and fast relaxation we must first determine the most probable path of excitation. Sahlberg et. al. [32, 60] have shown that strong LIGS signals in the mid-IR using water absorption are possible when the difference in a particular quantum number between the ground and excited states is non-zero [50]. The energy levels of an asymmetric top molecule like water can be expressed in terms of its rotational constants A, B, and C. The rotational energy levels $\epsilon(J, K_a, K_c)$ are given by:

$$\epsilon(J, K_a, K_c) = AK_a^2 + BJ(J+1) + CK_c^2$$
 (17)

where J is the total rotational quantum number, K_a and K_c are the quantum numbers associated with the projections of the rotational angular momentum on the principal axes. The values of A, B and C are equivalent to 27.88 cm⁻¹, 14.52 cm⁻¹ and 9.29 cm⁻¹, respectively [61, 62]. The R, P and Q branches involve transitions where Δ J = +1, -1 and 0, respectively. Using integration over the relevant energy range, one can determine the average rotational energy difference between all the possible states as $\Delta\epsilon_{\rm RT} = \frac{3}{4}{\rm A} + \frac{4}{3}{\rm B} + \frac{3}{4}{\rm C} = 47.24~{\rm cm}^{-1}$. The value of $\Delta\epsilon_{\rm VT}$ is approximated as 9398.50 cm⁻¹, based on the energy of the pump excitation wavelength. These values are



used in Eqs. 15 and 16. In section 4.3 we calculate the measured ratio value, *R*, for each condition under investigation.

4.3 Measured peak ratios

We now evaluate the second to first peak ratios from the experimental signals (see Fig. 2 (1) (a)). Figure 7 shows the measured ratio distributions for 1000 shots at each of the 55 locations for dry air (1) and the three premixed cases (2-4) described in Fig. 2. The height of the bar for each bin is normalised by the tallest bar in the histogram. The measured means and standard deviations are determined from the black solid Gaussian fits to each plot. Figure 7 (1) shows a measured mean and standard deviation for dry air ratios of $R_{\rm A(1)}=0.87~\pm~0.03$ (see Table 3). Due to zero moisture in dry air the signal is purely electrostrictive.

Figure 7 (2)-(4) shows histograms of the values of the ratio of second to first peak, R, for reactant and product ratios. The values are shown on Table 3 for the three reacting cases considered. The measured peak ratios for the reactants in all three cases are slightly larger than in the purely electrostrictive case of dry air, suggesting that there is some residual moisture in the compressed air. The fractional width of the measured ratio distributions is the same for all reactant and air values, corresponding to about 3% for all cases. We note that the ratio histogram has a wider distribution than the frequency histogram (frequency width was on the order of 1%). This is consistent with the fact that water molar fractions are primarily a function of temperature, and that temperature is proportional to the square of frequency.



Fig. 7 Normalised ratio histograms for LIGS signals measured at all locations. Each plot (1)-(4) contains the measured reactant ($R_{\rm R}$) and product ($R_{\rm P}$) ratios for the four conditions (1) dry air, (2) 100% CH₄, (3) 70% CH₄, and (4) 40% CH₄

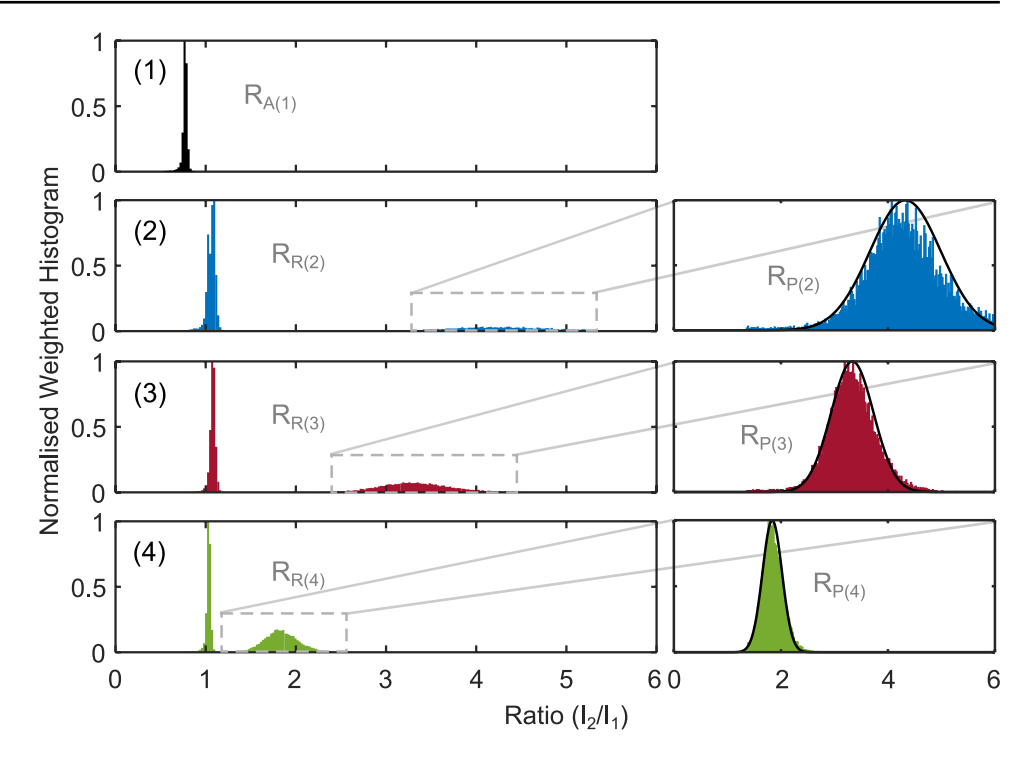


Table 3 Measured value of mean plus or minus standard deviations for the ratio R between second and first peak intensity of LIGS signals across all locations

Case	R _R (reactant)	R _P (product)
1 (dry air)	0.87 ± 0.03	_
2 (100% CH ₄)	1.07 ± 0.04	4.33 ± 0.66
3 (70% CH ₄)	1.07 ± 0.04 1.08 ± 0.03	3.34 ± 0.40
4 (40% CH ₄)	1.03 ± 0.03	$\frac{1.84 \pm 0.18}{1.84 \pm 0.18}$

In the absence of significant fluctuations in equivalence ratios, water vapour fluctuations should be twice as large as that of temperature.

The mean ratios measured in the product regions shown in detail on the right hand column of Fig. 7 decrease from case (2) to case (4). The result is consistent with a decrease in the total water molar fraction, as the overall equivalence ratio decreases (maintaining fixed power) from 0.60 to 0.39 (see Table 1). The standard deviation also decreases; the behaviour is discussed in section 4.4.

4.4 Calculating the water molar fraction

Sections 4.2 and 4.3 outlined the model (summarized in Eqs. 15 and 16) and experimental data describing the ratio of second to first peak. In LIGS signals we use $k \approx k_{N_2} = 2.38 \times 10^{-4} \text{ m}^3 \text{ kg}^{-1}$ [52] for the Gladstone-Dale constant and τ and τ_c to be equal to 10 ns [39] and 0 for the duration and coherence of the excitation pulses, respectively. The one factor still missing is τ_{VT} . In this section we discuss the method to determine $\tau_{\text{VT}} = \frac{1}{k_{\text{VT}}N_0}$

and outline how to fit mean measured ratios to the simulated ratios from the calculated temporal LIGS signatures described in section 4.1

Firstly we compute the equilibrium properties of dry air, reactants and products for the four experimental conditions under investigation using equilibrium calculations (Cantera 2.6.0 [44]) and thermodynamic properties (GRI Mech 3.0 [45]). These include the adiabatic flame temperatures, water molar fractions, molecular weights and specific heat ratios (see Table 2), densities, dynamic viscosity and diffusion constant values. Finally, using the fixed fringe spacing (from dry air speed of sound and temperature), one can calculate the angular frequency, $k_{\rm f}$ and $A_{\rm f}$ parameter for each condition.

The four time constants (thermal diffusion, acoustic damping, acoustic transit and molecular diffusion) are calculated using Eqs. 10, 11, 12 and 13. The characteristic times due to the diffusion and collisional relaxation are shortest, the acoustic decay times the longest, and the acoustic transit times are intermediate. All times are significantly shorter at high temperatures, leading to fewer peaks in the LIGS signals at high temperatures.

It is not possible to calculate the collisional relaxation time constant given by Eq. 14 as we do not know the value of $k_{\rm VT}$, which depends on the convolution function between the laser excitation, the detailed vibrational levels, and their transition probabilities. Therefore, we choose to fit the value of $\tau_{\rm VT}$ knowing the value of N_0 and using the constant $k_{\rm VT}$ as a variable. We then compute the ratio for the simulated signals and compare that to the ratios measured



experimentally. We then perform a least squares fit analysis to find the value of $\tau_{\rm VT}$ that causes the simulated ratio values to be the best match to the experimentally measured signals.

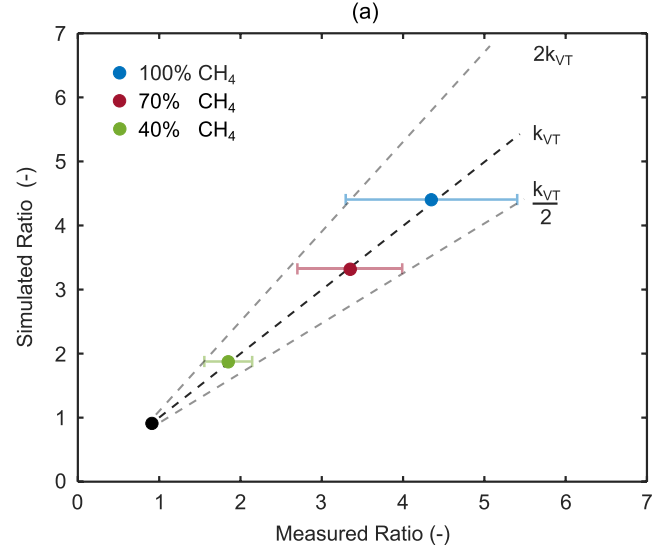
Figure 8 (a) shows the simulation results after minimising the error using a calculated value for parameter $k_{\rm VT}$, assumed to be the same for all mixtures. The value for $k_{\rm VT}$ is $2.35\times 10^{-17}~{\rm m}^3~{\rm s}^{-1}$. This gives fast (VT) molecular relaxation times of 3.5 ns, 3.3 ns and 2.8 ns for the products in the fuel blends (2) 100% CH₄, (3) 70% CH₄ and (4) 40% CH₄, respectively. The RT relaxation time is expected on the order of the characteristic binary collision timescale, which is instantaneous relative to the pulse duration and is on the order of 0.2 ns for 1 bar at 295 K [50].

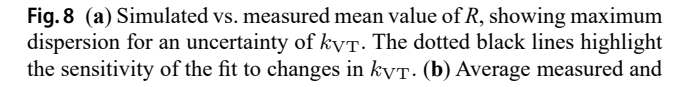
Figure 8 (b) shows the (solid coloured) measured average (of all three combustion cases) reactant (1) and product (2)-(4) normalised LIGS signatures, and the (solid black) calculated temporal evolution using the optimised parameters extracted from the fit. For the product spectra (2)-(4) we see excellent agreement between model and experiment. Any minor discrepancies likely result from experimental imperfections not captured in the model, such as the finite size of the laser beams causing acoustic energy loss. Nevertheless, it is remarkable how this relatively simple two-energy state simulation model captures the detailed and complex temporal behaviour for a range of LIGS signatures.

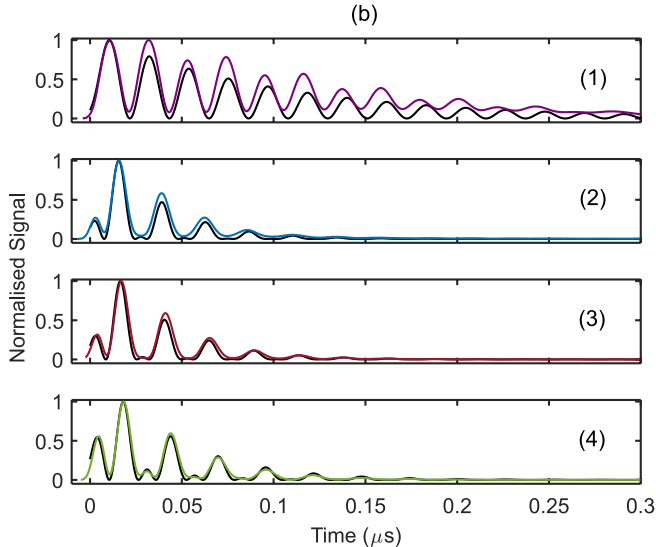
Finally, using calculated equilibrium values of water vapour concentrations, we can extract the values of water molar fractions for individual cases. Figure 9 (a) shows the mean measured values of the ratio for conditions 1-4 (dry air and 3 products for the different operating conditions), along with their corresponding standard deviations shown

as error bars. The simulated ratios are shown as colour lines. They intersect at the mean calibration condition used for determining the molar fraction. All cases converge to the limiting case for the fraction at dry air temperatures, showing a power behaviour associated with temperature, and low dependence on stoichiometry. The findings indicate that the previously used empirical linear models employed to connect water molar fractions and the ratio of thermal to electrostrictive signal peaks in premixed flames are not appropriate.

Figure 9 (b) (2)-(4) shows the calculated water molar fraction distributions across all locations for the three premixed cases described in Fig. 9 (a) (2)-(4). The mean calculated values are not significant, as they are used to obtain the necessary best-fit constants. However, note how the calculated vapour molar fraction distributions now show similar distribution widths (unlike the measured ratio values in section 4.3) of around ± 0.006 molar fractions. The dry air results represent an effective zero water molar fraction. However, the mean reactant water molar fractions are nonzero everywhere, as there is some mixing between reactants and products in the ORZ, along with entrainment of burned products from down stream regions via the extended IRZ. We also notice that in the case of reactants for case 2, there are two overlapping distributions, which may be due to the difference in mixing for pure methane (case 2) compared to methane-hydrogen blends (cases 3 and 4). Section 4.5 discusses the local variation of the molar fraction of water as a function of radial and axial locations.







calculated normalised temporal signals for different operating conditions. The solid black and coloured lines are the calculated and measured temporal signals, respectively



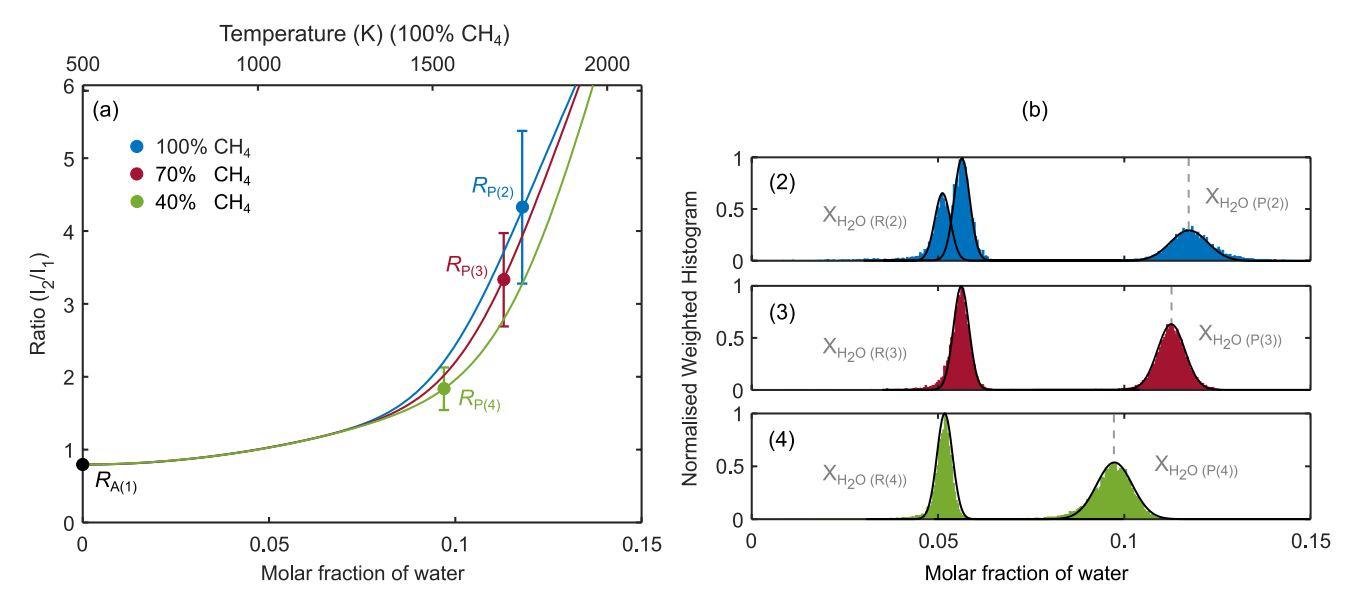


Fig. 9 (a) Simulated ratio values versus molar fractions of water and (b) calculated normalised water histograms for all measurement locations. The experimental ratios and errors bars from Table 3 are also plotted

4.5 Water vapour molar fraction spatial distributions

Figure 10 shows the calculated water molar fractions obtained from the ratio measurements, for the 100% CH₄ (blue), 70% CH₄ (red) and 40% CH₄ (green) cases at various radial and axial locations from the burner face. The intensity indicates the magnitude of the individual power spectrum intensities. The dotted grey lines correspond to the equilibrium water molar fractions for each combustion case (see Table 2). The grey solid regions highlight the location of the cylindrical quartz tube (measurements are taken at the centreline of the slots). The solid regions highlight the location of the flame brush. The lowest water fractions found near the inlet where we expect little water in the fresh reactants. Considering the evolution as a function of radial and axial position, we observe a few different characteristics depending on the case. The regions where water fractions transition from reactant to product overlap largely with the observed flame brush location.

For 100% CH₄ case (column (a)), calculated water fractions remain relatively constant in the IRZ. The temperature maps in section 3.6 did not indicate significant temperature rise in the ORZ, yet we observe increased water vapour concentrations in these regions. For the 70% CH₄ case (column (b)) there appears to be a band around radius 30-40 mm in which significant molar fractions of water vapour are present in the ORZ, suggesting recirculation of products into the reactants. Finally, for the 40% CH₄ case (column (c)) in which the flames are much shorter, the radial values around 40 mm also indicates recirculation, but the overall concentrations are lower. In section 5 we bring together both

temperature and molar fraction to understand the role of addition of hydrogen.

5 Frequency/temperature/ratio/water vapour correlations

Figure 11 (a) shows correlations of measured intensity ratios versus frequencies for the three premixed cases described in Fig. 2. The solid blue, red and green circles correspond to each of the combustion cases (2) 100% CH₄, (3) 70% CH₄ and (4) 40% CH₄, respectively. Frequencies below and above approximately 45 MHz correspond to thermal (T) and electrostrictive (E) frequencies, respectively, as indicated by the vertical dashed black boundary. For frequencies below 45 MHz, dominant (has a larger power spectra magnitude) thermal (DT) and minor thermal (MT) signatures correspond to ratios above and below the horizontal dashed black boundary. The opposite dependence is seen for frequencies above 45 MHz where dominant electrostrictive (DE) and minor electrostrictive (ME) signatures correspond to ratios below and above this line, respectively.

The dashed black line naturally splits the distributions from those where electrostriction is dominant versus thermal behaviour being dominant. For ratios below the dashed line the frequency of each mechanism can increase substantially with very little change to the overall measured ratio. However for ratios above the dashed line a small increase in frequency leads to a larger almost exponential increase in ratio. This is because these data points describe combustion phenomena in which the temperature is very closely related to the water concentration. Note that in the flame



201 Page 16 of 19 L. Weller et al.

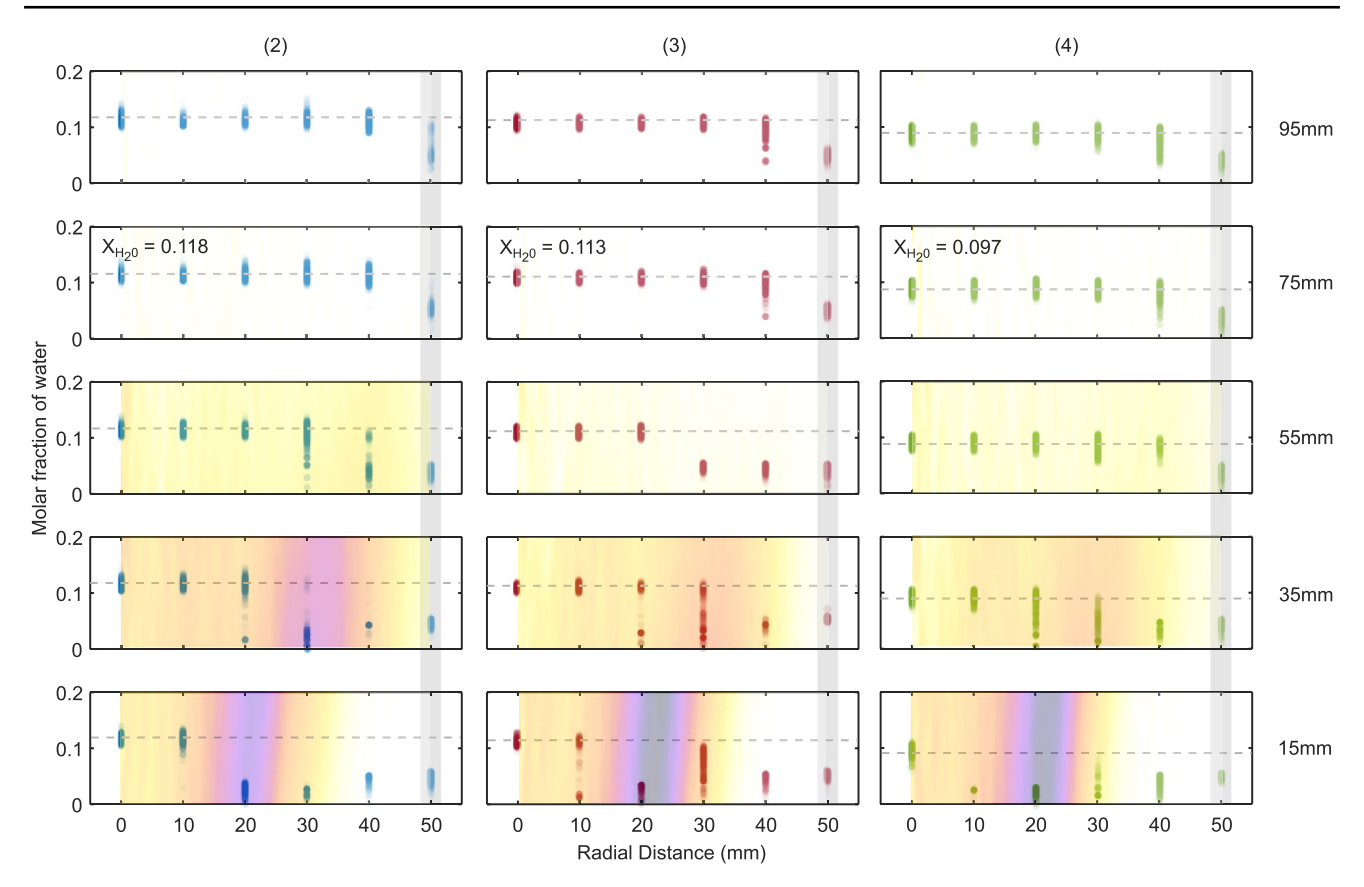


Fig. 10 Molar fraction of water vapour as a function of radial locations at axial distances of 15 mm, 35 mm, 55 mm, 75 mm and 95 mm from the burner edge. The colours indicate the three combustion cases (2) 100% CH₄ (blue), (3) 70% CH₄ (red) and (4) 40% CH₄ (green), respectively. The intensity indicates the magnitude of the individual

power spectrum intensities. The grey horizontal dotted lines correspond to the equilibrium water concentration for each combustion case. The grey vertical solid bands highlight the location of the cylindrical quartz tube enclosing the flame. The chemiluminescence images correspond to the flame brush regions shown in Fig 4.

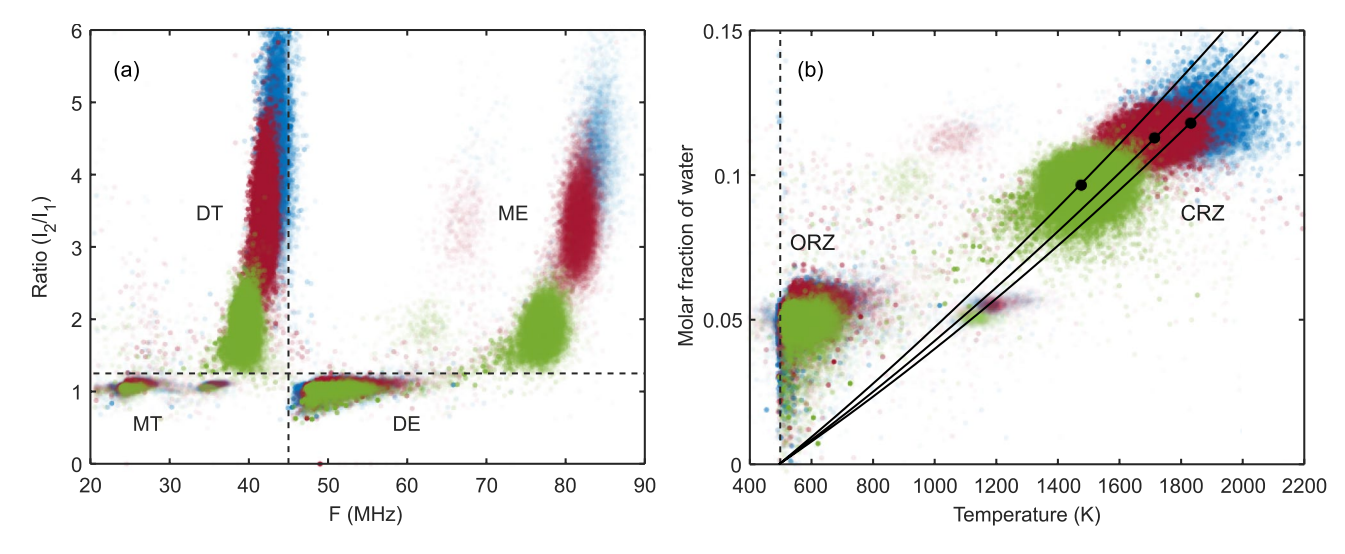


Fig. 11 (a) Measured ratio versus frequency values for the temporal LIGS signals in Fig. 2. The plot contains values for 100% CH₄ (blue), 70% CH₄ (red) and 40% CH₄ (green). Vertical and horizontal dashed black lines separate out the dominant and minor regimes for frequency and ratio, respectively. (b) Calculated water concentration versus temperature values for the temporal LIGS signals in Fig. 2. The plots

contain the values for 100% CH₄ (blue), 70% CH₄ (red) and 40% CH₄ (green). The black dotted line is the preheat temperature (500 K). The black circles and lines are the calculated equilibrium conditions and calculated water molar fractions versus temperature (see Table 2) for all three combustion cases



brush regions we measure frequencies around 30–40 MHz with ratios less than the dashed line, along with frequencies around 60–70 MHz with ratios more than the dashed line.

Figure 11 (b) shows the calculated molar fraction of water versus temperature for the three premixed cases described in Fig. 2. The vertical black dashed line corresponds to the preheat temperature of 500 K. The solid black circles correspond to the calculated equilibrium conditions (see Table 2) for each of the combustion cases (2 - blue circles) 100% $\rm CH_4$, (3 - red circles) 70% $\rm CH_4$ and (4 - green circles) 40% $\rm CH_4$ used for calibration. The solid black lines are the calculated molar fractions of water versus temperature using equilibrium simulations.

We note that in the product regions the water vapour molar fractions and temperatures agree well with the equilibrium simulations, as these values are used to calculate the simulated curves in section 4.4. Fluctuations are therefore not expected to be a result of changes in equivalence ratio, for example. The temperatures measured in the reactant zone show water vapour concentrations that are higher than expected from maximum saturation conditions for reactants (which would be around 2-3% at 500 K). Instead, we suggest that the higher concentrations are associated with recirculation of water vapour from the products to the base.

6 Conclusion

This study shows the first application of LIGS in high-pressure methane-hydrogen flames. The findings highlight the versatility of LIGS signals, which not only allow for the assessment of local temperature but also provide insights into local water concentration. This observation is particularly important in the context of pure hydrogen flames, where the combustion products consist solely of water and nitrogen. In addition, the present work suggests for the first time a quantitative method for accurate temperature and vapour concentration measurements using LIGS.

Measurements in the swirl-stabilised flame are made across radial and axial positions. These signals are analysed to extract both peak frequencies, which range from 20 to 90 MHz, and characteristic ratios of intensities of second to first peaks. Frequencies above and below 45 MHz, are classified as either electrostrictive or thermal, respectively. The peak frequencies are utilised to estimate temperatures, while the magnitudes of the first and second peaks in the signals are used to estimate water molar fractions. The uncertainties associated with each of these measurements are determined by assessing the spread in the probability density functions corresponding to the frequencies and intensities.

The experimental findings indicate that the previously used empirical linear models employed to connect water

molar fractions and the ratio of thermal to electrostrictive signal peaks in premixed flames are not appropriate. A new methodology was developed for this work, employing chemical equilibrium calculations and more sophisticated modelling of the LIGS signals to derive the non-linear relationship between water concentration and ratio parameter. Future work will improve this further by focussing on measurements in a controlled-environment such as a heated gas cell or a standard calibration flame, to fully assess the sensitivity and precision of the method for H₂O quantification across a range of conditions. Temperature and species measurements are then mapped across the domain to better understand the structure of these premixed swirling methane/hydrogen/air flames. For example, temperature values (derived from signal frequency) were unexpectedly high in some locations outside the flame brush but this was seen to correlate with an increase in the measured water concentration (derived from the ratio parameter). This supports the hypothesis of a recirculation process mixing combustion products with reactants near the base of the flame.

Although adding holes reduced reflections and improved signal extraction, it introduced unwanted air entrainment and mixing. Therefore two features to be modified in a future setup to overcome this difficulty are: (a) use thicker, flat surfaces to deliver the light rather than a curved tube. This has already been demonstrated in a recent study [63]. (b) alter the geometry of the beam relay, allowing for shorter focal length lenses to allow lower light intensity to cross the tube. This of course poses difficulties associated with organising the delivery of the beams in a compact unit. Finally, new developments in fs-LIGS may resolve some of these issues (but perhaps create new ones), by allowing significantly higher signal via multi-photon excitation.

The data allows us to gauge local mixture ratios within the combustion chamber, thereby enhancing our comprehension of the intricate dynamics in swirl-stabilized methane/hydrogen/air flames. Implementing LIGS in this setting not only provides valuable insights but also holds the promise of future applications in various industrial contexts where there is a demand for spatially resolved, real-time measurements of temperature and chemical species. This technology could prove essential in evaluating the stability and efficiency of systems powered by eco-friendly, carbonfree fuels.

Acknowledgements Lee Weller and Anthony Giles are funded under EPSRC UK Award EP/T030801/1 within the LIGS project. We thank Daniel Eakins and David Chapman for loan of the Coherent Verdi V-18 laser. We thank Priyav Shah for preparing the PILOT unit for testing and specifying the shape of the slots in the quartz tube. The dataset associated with this article is available from the corresponding author on request. For the purpose of open access, the author has applied a Creative Commons Attribution (CC BY) licence to any Author Accepted Manuscript version arising from this submission.



Author contributions L.W. designed the research, performed the experiment, analysed the data, prepared the figures, wrote the main manuscript, A.G. designed the research, performed the experiment, analysed the data, wrote the main manuscript, O.C. performed the experiment, analysed the data, S.M. designed the research, performed the experiment, B.A.O.W. designed the research, wrote the main manuscript, S.H. designed the research, wrote the main manuscript, all authors reviewed the manuscript.

Data availability No datasets were generated or analysed during the current study.

Declarations

Conflict of interest The authors declare no Conflict of interest.

Open Access This article is licensed under a Creative Commons Attribution 4.0 International License, which permits use, sharing, adaptation, distribution and reproduction in any medium or format, as long as you give appropriate credit to the original author(s) and the source, provide a link to the Creative Commons licence, and indicate if changes were made. The images or other third party material in this article are included in the article's Creative Commons licence, unless indicated otherwise in a credit line to the material. If material is not included in the article's Creative Commons licence and your intended use is not permitted by statutory regulation or exceeds the permitted use, you will need to obtain permission directly from the copyright holder. To view a copy of this licence, visit http://creativecommons.org/licenses/by/4.0/.

References

- S.R. Bell, M. Gupta, Extension of the lean operating limit for natural gas fueling of a spark ignited engine using hydrogen blending. Combust. Sci. Technol. 123(1-6), 23-48 (1997)
- F. Halter, C. Chauveau, I. Gökalp, Characterization of the effects of hydrogen addition in premixed methane/air flames. Int. J. Hydrogen Energy 32(13), 2585–2592 (2007)
- R. Schefer, Hydrogen enrichment for improved lean flame stability. Int. J. Hydrogen Energy 28(10), 1131–1141 (2003)
- A. Degenève, C. Mirat, J. Caudal, R. Vicquelin, T. Schuller, Effects of swirl on the stabilization of non-premixed oxygenenriched flames above coaxial injectors. J. Eng. Gas Turbines Power 141(12), 121018 (2019)
- H. Tang, C. Yang, G. Wang, T.F. Guiberti, G. Magnotti, Raman spectroscopy for quantitative measurements of temperature and major species in high-pressure non-premixed nh3/h2/n2 counterflow flames. Combust. Flame 237, 111840 (2022)
- I.R.Lewis, H.Edwards, Handbook of raman spectroscopy: from the research laboratory to the process line (2001)
- 7. A.C.Eckbreth, Laser diagnostics for combustion temperature and species **3** (1996)
- R.S. Barlow, M.J. Dunn, M.S. Sweeney, S. Hochgreb, Effects of preferential transport in turbulent bluff-body-stabilized lean premixed ch4/air flames. Combust. Flame 159(8), 2563–2575 (2012)
- V.B.Mbayachi, Z.-Y.Tian, X.Zhang, M.Khalil, D.A.Ayejoto, Laser-induced fluorescence in combustion research, 223–243 (2023)
- J. Kiefer, P. Ewart, Laser diagnostics and minor species detection in combustion using resonant four-wave mixing. Prog. Energy Combust. Sci. 37(5), 525–564 (2011)

- M.Gutfleisch, D.Shin, T.Dreier, P.Danehy, Mid-infrared laser-induced grating experiments of C2H4 and nh3 from 0.1–2 Mpa and 300–800 K. Appl. Phys. B 71(5), 673–680 (2000)
- 12. R. Stevens, P. Ewart, Single-shot measurement of temperature and pressure using laser-induced thermal gratings with a long probe pulse. Appl. Phys. B **78**(1), 111–117 (2004)
- Y. Wu, M. Zhuzou, T. Zhao, P. Ding, S. Sun, J. Wang, Z. Liu, B. Hu, Gas-phase pressure measurement using femtosecond laser-induced grating scattering technique. Opt. Lett. 47(7), 1859–1862 (2022)
- C. Willman, L.M. Le Page, P. Ewart, B.A. Williams, Pressure measurement in gas flows using laser-induced grating lifetime. Appl. Opt. 60(15), 131–141 (2021)
- A. Too, E. Sidiropoulos, Y. Holz, N.W. Karuri, T. Seeger, Dualpump vibrational coherent anti-stokes raman scattering system developed for simultaneous temperature and relative nitrogenwater vapor concentration measurements. Optics 4(4), 613–624 (2023)
- L. Castellanos, F. Mazza, A. Bohlin, Water vapor in hydrogen flames measured by time-resolved collisional dephasing of the pure-rotational n2 cars signal. Proc. Combust. Inst. 39(1), 1279– 1287 (2023)
- E. Nordström, A. Bohlin, P.-E. Bengtsson, Pure rotational coherent anti-stokes raman spectroscopy of water vapor and its relevance for combustion diagnostics. J. Raman Spectrosc. 44(10), 1322–1325 (2013)
- F. De Domenico, T.F. Guiberti, S. Hochgreb, W.L. Roberts, G. Magnotti, Temperature and water measurements in flames using 1064 nm laser-induced grating spectroscopy (ligs). Combust. Flame 205, 336–344 (2019)
- 19. E. Cummings, Laser-induced thermal acoustics: simple accurate gas measurements. Opt. Lett. 19(17), 1361–1363 (1994)
- E. Cummings, I. Leyva, H. Hornung, Laser-induced thermal acoustics (lita) signals from finite beams. Appl. Opt. 34(18), 3290–3302 (1995)
- P.H. Paul, R.L. Farrow, P.M. Danehy, Gas-phase thermal-grating contributions to four-wave mixing. JOSA B 12(3), 384–392 (1995)
- 22. A. Stampanoni-Panariello, D.Kozlov, P. Radi, B.Hemmerling, Gas phase diagnostics by laser-induced gratings i. Theory. Appl. Phys. B 81(1), 101–111 (2005)
- W. Hubschmid, B. Hemmerling, A. Stampanoni-Panariello, Rayleigh and brillouin modes in electrostrictive gratings. JOSA B 12(10), 1850–1854 (1995)
- 24. A. Stampanoni-Panariello, B.Hemmerling, W.Hubschmid, Temperature measurements in gases using laser-induced electrostrictive gratings. Appl. Phys. B: Lasers & Optics **67**(1) (1998)
- D. Kozlov, Simultaneous characterization of flow velocity and temperature fields in a gas jet by use of electrostrictive laserinduced gratings. Appl. Phys. B 80(3), 377–387 (2005)
- A.Stampanoni-Panariello, D.Kozlov, P.Radi, B.Hemmerling, Gas-phase diagnostics by laser-induced gratings ii, experiments. Appl. Phys. B 81(1), 113–129 (2005)
- H.J.Eichler, P.Günter, D.W.Pohl, Laser-induced dynamic gratings 50 (2013)
- S. Williams, L.A. Rahn, P.H. Paul, J.W. Forsman, R.N. Zare, Laser-induced thermal grating effects in flames. Opt. Lett. 19(21), 1681–1683 (1994)
- M.S.Brown, W.L.Roberts, Thermometry in pressurized sooting flames using laser-induced gratings. In: Optical Technology in Fluid, Thermal, and Combustion Flow III, vol. 3172, pp. 492–503 (1997). SPIE
- A.-L. Sahlberg, D. Hot, J. Kiefer, M. Aldén, Z. Li, Mid-infrared laser-induced thermal grating spectroscopy in flames. Proc. Combust. Inst. 36(3), 4515–4523 (2017)



- A.Hayakawa, T.Yamagami, K.Takeuchi, Y.Higuchi, T.Kudo, S.Lowe, Y.Gao, S.Hochgreb, H.Kobayashi, Quantitative measurement of temperature in oxygen enriched CH4/O2/N2 premixed flames using laser induced thermal grating spectroscopy (litgs) up to 1.0 mpa. Proceedings of the Combustion Institute 37(2), 1427–1434 (2019)
- D. Hot, A.-L. Sahlberg, M. Aldén, Z. Li, Mid-infrared laser-induced thermal grating spectroscopy of hot water lines for flame thermometry. Proc. Combust. Inst. 38(1), 1885–1893 (2021)
- 33. M.S. Brown, Y. Li, W.L. Roberts, J.R. Gord, Analysis of transient-grating signals for reacting-flow applications. Appl. Opt. **42**(3), 566–578 (2003)
- 34. L.Weller, P.Shah, A.Giles, F.De Domenico, S.Morris, B.A.Williams, S.Hochgreb, Spatial temperature and water molar concentration measurements using thermal and electrostrictive ligs during operation of a swirl burner at pressure. In: Turbo Expo: Power for Land, Sea, and Air, 86977, 04–05004 (2023). American Society of Mechanical Engineers
- L. Weller, P. Shah, A. Giles, F. Domenico, S. Morris, B.A.O. Williams, S. Hochgreb, Spatial temperature and water molar concentration measurements using thermal and electrostrictive ligs during operation of a swirl burner at pressure. J. Eng. Gas Turbines Power 146(5), 051021 (2023). https://doi.org/10.1115/1.4063865
- Y. Wu, P. Ding, Y. Zheng, T. Zhao, Z. Zhu, X. Liu, S. Sun, J. Wang, Z. Liu, B. Hu, Characterization of femtosecond laser-induced grating scattering of a continuous-wave laser light in air. Opt. Express 30(10), 17038–17053 (2022)
- J. Chen, R. Yang, L. Chen, Z. Hao, J. Wang, S. Sun, Z. Liu, B. Hu,
 P. Ding, Simultaneous measurement of temperature and pressure using deep-learning-assisted femtosecond laser-induced scattering technique. Opt. Express 33(11), 23740–23754 (2025)
- M. Ruchkina, D. Hot, P. Ding, A. Hosseinnia, P.-E. Bengtsson, Z. Li, J. Bood, A.-L. Sahlberg, Laser-induced thermal grating spectroscopy based on femtosecond laser multi-photon absorption. Sci. Rep. 11(1), 9829 (2021)
- 39. P. Shah, L.M. Le Page, B.A. Williams, Development and characterization of pilot: a transportable instrument for laser-induced grating spectroscopy. Opt. Express 31(4), 5872–5881 (2023)
- O.Chaib, L.Weller, A.Giles, S.Morris, B.A.O.Williams, S.Hochgreb, Spatial Temperature Measurements in a Swirl-Stabilized Hydrogen-Air Diffusion Flame At Elevated Pressure Using Laser-Induced Grating Spectroscopy. J. Eng. Gas Turbines Power, 1–13 (2024) https://doi.org/10.1115/1.4065996
- 41. J. Runyon, R. Marsh, P. Bowen, D. Pugh, A. Giles, S. Morris, Lean methane flame stability in a premixed generic swirl burner: isothermal flow and atmospheric combustion characterization. Exp. Thermal Fluid Sci. 92, 125–140 (2018)
- 42. D.Pugh, P.Bowen, A.Crayford, R.Marsh, J.Runyon, S.Morris, A.Giles, Catalytic influence of water vapor on lean blow-off and nox reduction for pressurized swirling syngas flames. J. Eng. Gas Turbines Power **140**(6) (2018)
- D. Pugh, P. Bowen, A. Valera-Medina, A. Giles, J. Runyon, R. Marsh, Influence of steam addition and elevated ambient conditions on nox reduction in a staged premixed swirling nh3/h2 flame. Proc. Combust. Inst. 37(4), 5401–5409 (2019)
- D.G.Goodwin, R.L.Speth, H.K.Moffat, B.W.Weber, Cantera: An object-oriented software toolkit for chemical kinetics, thermodynamics, and transport processes. Version 2.6.0 (2023)
- G.P. Smith, D.M.Golden, M.Frenklach, N.W.Moriarty, B.Eiteneer, M.Goldenberg, C.T.Bowman, R.K.Hanson, S.Song, W.C.Gardiner Jr, et al.: Gri 3.0 mechanism, gas research institute, 1999. http://www.me. berkeley. edu/gri_mech
- J. Runyon, R. Marsh, Y.A. Sevcenco, D. Pugh, S. Morris, Development and commissioning of a chemiluminescence imaging

- system for an optically-accessible high-pressure generic swirl burner (2015)
- C.J. Dasch, One-dimensional tomography: a comparison of abel, onion-peeling, and filtered backprojection methods. Appl. Opt. 31(8), 1146–1152 (1992)
- 48. B. Hemmerling, D. Kozlov, Collisional relaxation of singlet o2 (b1σ Collisional relaxation of singlet o2 (b1σ+ g) in neat gas investigated by laser-induced grating technique g) in neat gas investigated by laser-induced grating technique. Chem. Phys. 291(3), 213–242 (2003)
- D.N. Kozlov, J. Kiefer, T. Seeger, A.P. Froeba, A. Leipertz, Determination of physicochemical parameters of ionic liquids and their mixtures with solvents using laser-induced gratings. J. Phys. Chem. B 115(26), 8528–8533 (2011)
- B. Hemmerling, D. Kozlov, O. Stel'makh, B. Attal-Trétout, Diagnostics of water-containing gas mixtures using thermal laser-induced gratings. Chem. Phys. 320(2–3), 103–117 (2006)
- E. Loubignac, B. Attal-Trétout, S. Le Boiteux, D. Kozlov, Twocolor non-linear spectroscopy: application to no2. Comptes Rendus de l'Académie des Sciences-Series IV-Physics 2(7), 1013–1027 (2001)
- S.J. Grauer, A. Unterberger, A. Rittler, K.J. Daun, A.M. Kempf, K. Mohri, Instantaneous 3d flame imaging by background-oriented schlieren tomography. Combust. Flame 196, 284–299 (2018)
- C.T. Wanstall, A.K. Agrawal, J.A. Bittle, Implications of real-gas behavior on refractive index calculations for optical diagnostics of fuel-air mixing at high pressures. Combust. Flame 214, 47–56 (2020)
- W. Gardiner Jr., Y. Hidaka, T. Tanzawa, Refractivity of combustion gases. Combust. Flame 40, 213–219 (1981)
- V.Lang, OPERATIONS, A.C.E.S.C.T.: Relaxation processes of vibrationally excited h 2 o in the mesosphere and thermosphere. Unknown (1991)
- R. Manuilova, A. Feofilov, A. Kutepov, V. Yankovsky, Effect of updated relaxation rate constants on the h2o vibrational level populations and ro-vibrational spectra in the mesosphere and lower thermosphere. Adv. Space Res. 56(9), 1806–1814 (2015)
- 57. P. Zittel, D. Masturzo, Vibrational relaxation of h2o from 295 to 1020 k. J. Chem. Phys. **90**(2), 977–989 (1989)
- M. Braunstein, P.F. Conforti, Classical dynamics of h2o vibrational self-relaxation. J. Phys. Chem. A 119(14), 3311–3322 (2015)
- C.S.Goldenstein, V.A.Miller, R.M.Spearrin, C.L.Strand. Spectraplot. com: Integrated spectroscopic modeling of atomic and molecular gases. Journal of Quantitative Spectroscopy and Radiative Transfer 200, 249–257 (2017)
- A.-L. Sahlberg, D. Hot, R. Lyngbye-Pedersen, J. Zhou, M. Aldén,
 Z. Li, Mid-infrared polarization spectroscopy measurements of species concentrations and temperature in a low-pressure flame.
 Appl. Spectrosc. 73(6), 653–664 (2019)
- G.Herzberg, Molecular spectra and molecular structure-vol i 1 (2013)
- H. Pickett, R. Poynter, E. Cohen, M. Delitsky, J. Pearson, H. Müller, Submillimeter, millimeter, and microwave spectral line catalog. J. Quant. Spectrosc. Radiat. Transfer 60(5), 883–890 (1998)
- 63. A.Giles, L.Weller, B.Göktepe, O.Chaib, P.Shah, B.Williams, A.Crayford, D.Pugh, S.Hochgreb. Operability study with spatial resolved temperature and water molar concentration measurements of a new pressurised optical modular staged combustor. In: Turbo Expo, 88780, 03–04023 (2025). American Society of Mechanical Engineers

Publisher's Note Springer Nature remains neutral with regard to jurisdictional claims in published maps and institutional affiliations.

